



저작자표시-비영리-변경금지 2.0 대한민국

이용자는 아래의 조건을 따르는 경우에 한하여 자유롭게

- 이 저작물을 복제, 배포, 전송, 전시, 공연 및 방송할 수 있습니다.

다음과 같은 조건을 따라야 합니다:



저작자표시. 귀하는 원저작자를 표시하여야 합니다.



비영리. 귀하는 이 저작물을 영리 목적으로 이용할 수 없습니다.



변경금지. 귀하는 이 저작물을 개작, 변형 또는 가공할 수 없습니다.

- 귀하는, 이 저작물의 재이용이나 배포의 경우, 이 저작물에 적용된 이용허락조건을 명확하게 나타내어야 합니다.
- 저작권자로부터 별도의 허가를 받으면 이러한 조건들은 적용되지 않습니다.

저작권법에 따른 이용자의 권리는 위의 내용에 의하여 영향을 받지 않습니다.

이것은 [이용허락규약\(Legal Code\)](#)을 이해하기 쉽게 요약한 것입니다.

[Disclaimer](#)

공학박사 학위논문

Control of Coloration and Colloidal Assembly Based on Molecular Ordering of Reactive Mesogens

반응성 메소겐의 분자질서를 이용한 색 제어 및
콜로이드 조립에 관한 연구

2016 년 8 월

서울대학교 대학원

공과대학 전기·컴퓨터공학부

김 세 움

Control of Coloration and Colloidal Assembly Based on Molecular Ordering of Reactive Mesogens

지도 교수 이 신 두

이 논문을 공학박사 학위논문으로 제출함
2016 년 8 월

서울대학교 대학원
공과대학 전기·컴퓨터공학부
김 세 움

김세움의 공학박사 학위논문을 인준함
2016 년 6 월

위 원 장 _____ 이 창 희 (인)

부위원장 _____ 이 신 두 (인)

위 원 _____ 홍 용 택 (인)

위 원 _____ 유 창 재 (인)

위 원 _____ 최 윤 석 (인)

Abstract

In recent years, reactive mesogens (RMs) have attracted much attention due to their intrinsic anisotropy as well as a capability of forming highly stable liquid crystalline polymer by a polymerization process. The extended functionality of RM such as photo-sensitivity and thermal-sensitivity can be provided in a simple way of modifying the molecular structure or combining various functional fragments. In addition, the RM films are easily formed onto various kinds of substrate by a solution process. The surface characteristics of the RM structures strongly depend on the molecular alignment of the RMs. Such dependency was hardly observed from the isotropic polymer structures.

In this thesis, new types of electro-optical devices and the directional assembly of the colloidal particles using aligning capability of RMs were proposed. At first, the liquid crystal (LC) aligning capability of the RM was experimentally examined in the LC/RM composite system where the patterned RM structures were formed on the bottom substrate of LC cell. In the LC/isotropic polymer composite system, the alignment LC molecules was often distorted due to the monotonic directional preference on the surface of the isotropic polymer structure. On the other hand, the directional preference of LC on the RM structure is identical to the molecular

orientation of RM so that the highly uniform alignment of LC molecules across the RM patterns can be achieved by molecular ordering of RM. Next, the surface-initialized polymer stabilization of RM was studied. In usual polymer stabilization process, the photo-initiator was doped directly in the RM/LC mixture. Therefore, the spontaneous polymerization process occurred in the entire region exposed to the external energy. In the approach proposed here, the photo-initiator was doped on the one side of the alignment layer to induce the surface-initialized photo-polymerization. Thus, both the pure LC layer and stabilized RM/LC layer can coexist in a stacking configuration. This concept is directly applicable for electro-optical devices requiring high electrical tunability. Moreover, the self-organized surface topography of the RM film was studied. The depth-wise gradient polymerization of swelled RM film generates the buckling instability to form the surface topography in range from nano to micro scale. It was found that the directional preference of the surface topography appeared when the RM is uniformly aligned before polymerization.

Based on the results described above, a new concept of reflective-type liquid crystal display (RLCD) based on the polarization selective reflector (PSR) was proposed. Previously, the color filter was placed in front of the RLCD and the mirror was constructed on the bottom substrate. In such configuration, the ambient light passes the different color filters during incidence and reflection depending on the incident angle. In the proposed approach here, the PSR on the bottom substrate acts as a role of polarization-selective mirror as well as color filter so that the color loss from the filtration can be effectively reduced. The PSR was constructed through the spin-coating of chiral nematic RM mixture and photo-polymerization process with the photomask. The PSR selectively reflects the circular polarization

component of incident light in the pre-defined bandwidth of the wavelength and the reflectance can be varied by the applied voltage to change the phase retardation of the upper LC layer.

Next, a new way of reducing color distortion in liquid crystal display (LCD) based on anisotropic voltage dividing layer (AVDL) was demonstrated. The voltage dividing layer (VDL)-based method for reducing color distortion involved a planarization processes for the uniform alignment of LC molecules on the VDL. The proposed approach based on AVDL enables to spontaneously align the LC molecules without any additional surface treatment. The color distortion of the LCD in patterned vertical alignment mode was examined by both numerical simulations and the experimental measurements.

Finally, the assembly of the colloidal microwires using self-organized surface topography was demonstrated. The surface topography of highly uniform wavy structure was formed along the direction of RM. Using the periodic wavy structures as the templates, the colloidal microwires in single line or multiple lines were assembled. The number of lines was determined depending on the height and the period of the wrinkle in combination with the particle size.

In conclusion, the anisotropic aligning capability of RM was explored for the control of the coloration and the directional colloidal assembly. The new concept of device and both theoretical and experimental results provided here will lead to the development of the advanced electro-optical device and the colloid applications.

Keywords: liquid crystal, reactive mesogen, liquid crystal display, reflective liquid crystal display, liquid crystal/reactive mesogen composite system, colloidal assembly, self-organized surface topography.

Student number: 2010-20771

Contents

Abstract	i
Contents	v
List of Figures	viii
List of Tables	xvii
Chapter 1 Introduction	1
1.1 Liquid Crystals	1
1.2 Reactive Mesogens	8
1.3 Outline of Thesis	11
Chapter 2 Aligning Capability of Reactive Mesogens	15
2.1 Introduction	15
2.2 Liquid Crystal/Reactive Mesogen Composite Systems	16
2.2.1 Liquid crystals on patterned reactive mesogen film	16
2.2.2 Stabilization of liquid crystals by reactive mesogen	24
2.4 Self-Organized Surface Topography of Reactive Mesogen	34
2.5 Summary	44

Chapter 3 Tunable Color Elements Based on Chiral Reactive Mesogens	46
3.1 Introduction	46
3.2 Operation Principle	47
3.3 Fabrication Process	57
3.4 Results and Discussion	59
3.5 Summary	68
Chapter 4 Reduction of Color Shift by Reactive Mesogen Layer	70
4.1 Introduction	70
4.2 Operation Principle	72
4.3 Numerical Calculation	73
4.3.1 Theoretical description	74
4.3.2 Simulation result of gamma distortion	76
4.4 Experiment	82
4.4.1 Fabrication process	82
4.4.2 Results and discussion	85
4.5 Summary	92
Chapter 5 Colloidal Assembly on Wrinkled Template of Reactive Mesogen	93
5.1 Introduction	93
5.2 Templates with Wrinkled Patterns of Reactive Mesogen	94
5.3 Construction of Colloidal Microwires	100
5.4 Summary	103
Chapter 6 Concluding Remarks	104
Bibliography	107

Publication	115
국문 초록	123

List of Figures

Figure 1.1. Schematic illustration of nematic (N), smectic A (SmA), and smectic C (SmC) phases.	3
Figure 1.2. Schematic illustration of the chiral nematic (N*) phase.	6
Figure 1.3. Schematic illustration of the chiral smectic (SmC*) phase.	8
Figure 1.4. Schematic illustration of (a) the RM and (b) the LCP formed by the polymerization of the RM.	10
Figure 2.1. Fabrication process of LC cell with the RM patterns on the bottom substrate. (a) Spin-coating of the RM on the alignment layer. (b) Photo-polymerization process with the photomask. (c) Wash out process for the removal of un-polymerized RM. (d) Construction of the cell and the infiltration of LC.	18
Figure 2.2. Fabrication process of LC cell with the isotropic patterns on the bottom substrate. (a) Spin-coating of alignment layer on the glass substrate. (b) Contact of PDMS mold deposited with fluorinated polymer on the alignment layer. (c) Transfer-printed fluorinated polymer patterns. (d) Construction of the cell and	

the infiltration of LC.	20
Figure 2.3. (a)-(d) Microscopic images of LC cell with the RM patterns on the bottom substrate. (a), (b) Horizontally aligned LC cell. Here, <i>A</i> , <i>P</i> , and <i>R</i> denote the analyzer, the polarizer, and the rubbing direction, respectively. (c), (d) Vertically aligned LC cell. (e) Microscopic images of vertically aligned LC cell with the fluorinated polymer patterns on the bottom substrate.	22
Figure 2.4. Schematic diagram of the directional preference of LC and the resultant alignment of LC near (a) the isotropic pattern and (b) the anisotropic pattern.	23
Figure 2.5. Schematic diagram showing the fabrication process of the polymer stabilized LC cell based on the polymer network. (a) Cell filled with the chiral mixture. Here, one alignment layer was doped with the photo-initiator. (b) Photo-polymerization by the UV exposure. Bottom substrate faces the photomask (c) Wash out process for the removal of chiral mixture. (d) Infiltration of nematic LC.	26
Figure 2.6. SEM images of the part of polymer networks formed on the bottom substrate using M_1 at the UV exposure times of (a) 20 s, (b) 40 s, (c) 60 s, and (d) 80 s.	28
Figure 2.7. SEM images of the part of polymer networks formed on the bottom substrate using (a) M_1 , (a) M_2 , (a) M_3 , and (a) M_4 at	

the 80 s of the UV exposure times.	29
Figure 2.8. Thickness of the polymer network produced from four mixtures as a function of UV exposure time.	30
Figure 2.9. Microscopic images of the sample cell at each fabrication step using M ₂ . (a) The initial state filled with the M ₂ . (b) The photo-polymerization process. (c) The wash out process. (d) The re-infiltration of LC. (e) The thermal treatment. (f) The optical spectra of the corresponding state shown in (a) ~ (e).	31
Figure 2.10. Microscopic images of the sample cell at each fabrication step using M ₄ . (a) The initial state filled with the M ₄ . (b) The photo-polymerization process. (c) The wash out process. (d) The re-infiltration of LC. (e) The thermal treatment. (f) The optical spectra of the corresponding state shown in (a) ~ (e).	33
Figure 2.11. Schematic diagram showing the surface topography of the monomer film. (a) Plasma treatment on the surface of the monomer film. (b) The thermal swelling of the monomer film. (c) The depth-wise gradient polymerization. (d) The surface topography induced by the buckling instability after the cooling of the monomer film.	36
Figure 2.12. Schematic diagram showing the multi-directional rubbing process and the deposition of the RM film. (a) The alignment layer was firstly rubbed along the direction R_1 . (b) Transfer printing of the fluorinated polymer as a screening layer	

preserving the first rubbing during the second rubbing along R_2 .
(c) Lift-off process of the screening layer. The multi-domains with the directional preference in R_1 or R_2 were formed. (d) The RM film was deposited by the spin-coating of the RM mixtures in solvent. 39

Figure 2.13. Three different rubbing conditions of the alignment layer and the microscopic images of the RM film coated on the corresponding alignment layer. (a) The un-rubbed alignment layer and the randomly formed wrinkles. (b) The rubbed alignment layer along the direction R_1 and the aligned wrinkles along the rubbing direction. (c) The multi-directionally rubbed alignment layer with the help of the screening layer and the wrinkles aligned in the two directions. 41

Figure 2.14. (a), (b) AFM images of the nanobumps on the RM film with the small depth-wise gradient of the polymerization. (c), (d) Microscopic images of the well-organized wrinkles along one direction on the RM film with the large depth-wise gradient of the polymerization. Black dotted arrows represent the rubbing direction of the alignment layer. 43

Figure 3.1. Schematic diagram illustrating the operation principle of RLCD based on the PSR of the CRM. (a) The initial dark state with the homogeneous alignment of LC where the reflected light blocked by the front polarizer. (b) The state of applied

voltage with the reduction of phase retardation at the LC layer.

The reflected light comes out from the device. 49

Figure 3.2. Schematic diagram of optical pathways for (a) the initial off state and (b) the state of arbitrary on state by the applied voltage. Here, the red arrows and the blue arrows represent the propagation of incident light and reflected light, respectively and the dashed arrows represent the transition of polarization. 56

Figure 3.3. Fabrication process of the RLCD based on the PSR of the CRM. (a) Spin-coating of M_R on the prepared bottom ITO substrate. (b) Photo-polymerization of the M_R layer using the photomask. (c) Wash-out process for the removal of the residual material. (d) Repetition using M_G and M_B in sequence. (e) Construction of the cell and the infiltration of LC. 59

Figure 3.4. Microscopic images of the reflection of (a) R, (b) G, and (c) B by the PSR array in a rectangular shape depending on the applied voltage. 61

Figure 3.5. The normalized voltage-dependent reflectance of the (a) R, (b) G, and (c) B elements. 64

Figure 3.6. Dynamic response of the cell based on the PSR-R. 64

Figure 3.7. Optical spectrum of the (a) R, (b) G, and (c) B depending on the applied voltage. 66

Figure 3.8. Microscopic images for the prototype demonstration of the proposed RLCD incorporated with the three PSR for the

primary colors of R, G, and B. 68

Figure 4.1. The conceptual diagrams of the LC cell with (a) the IVDL and (b) the AVDL in the vertical alignment mode. Here, d_1 , d_2 denote the thickness of the AVDL and that of the LC layer in the bulk, respectively. The microscopic textures were taken under crossed polarizers (*A*: analyzer and *P*: polarizer). 73

Figure 4.2. The schematic illustration of the top views of the LC unit cells (a) without the AVDL (4-domain) and (b) with the AVDL (8-domain). Black lines and dotted lines represent the bottom and top electrodes, respectively. The direction and the amount of tilt angle of the LC in the sub-domains are represented by the arrows. Red lines represent the cross-section lines for two-dimensional simulations. The cross sectional view of a unit cell with the AVDL is shown in the bottom of (b). (c) A symmetric unit cell corresponding to the cross-section along the red line for two-dimensional simulations. Black dotted lines in the cell represent the electrical field lines. Here, the geometrical parameters are given in the unit of μm 78

Figure 4.3. Simulation results for the luminance as a function of the input grey level (gamma curves) for different values of the polar angles ($\theta = 0^\circ$ to 60° at $\varphi = 0^\circ$) for (a) $d_1 = 0$ and (b) $d_1 = 0.6 \mu\text{m}$. (c) The calculated GDI as a function of the AVDL thickness for different polar angles from 0° to 60° . The range of

the proper thickness of the AVDL for the effective reduction of
the GDI value is represented by the region in red. 81

Figure 4.4. Schematic diagram showing the fabrication process of the PVA LC cell based on the AVDL. (a) The patterned ITO glass. Here, w_1 , w_2 , and h are 12 μm , 63 μm , and 150 μm , respectively. The shape of the electrode is identical to the simulation geometry. (b) Deposition of the homeotropic alignment layer by the spin-coating process. (c) Deposition of RM by the spin-coating process. (d) Photo-polymerization of RM and wash out process for removal the un-polymerized RM. (e) Construction of the cell with the top patterned ITO glass with the homeotropic alignment layer. (f) Infiltration of LC. 84

Figure 4.5. (a) Contact angles of deionized water and ethylene glycol together with the corresponding surface energy of the AVDL a function of the UV exposure time. (b) Microscopic textures of the vertical alignment mode LC cell with periodic AVDLs prepared under four different UV exposure times of 30, 60, 90, and 120 s. Insets show the AFM images of the AVDLs. The values of the surface roughness for the ADVLs were 1.292 nm, 1.288 nm, 1.332 nm, and 1.603 nm. The microscopic textures were taken under crossed polarizers. Scale bars in the inset are 2 μm 86

Figure 4.6. (a) The simulation results and (b) the experimental results

for the voltage-dependent transmittance of the vertical alignment mode LC cells with different values of the AVDL thickness. 88

Figure 4.7. (a) Microscopic images of the PVA LC cell with periodic AVDLs ($d_1 = 0.57 \mu\text{m}$) at various applied voltages of 0, 2.5, 3.0, 3.5, 4.0, and 5.0 V. The microscopic textures were taken under crossed polarizers. 89

Figure 4.8. Experimental results for the luminance as a function of the input grey level (gamma curves) for (a) $d_1 = 0 \mu\text{m}$ and (b) $d_1 = 0.57 \mu\text{m}$. (c) Measured values of the GDI in the case of $d_1 = 0 \mu\text{m}$ and $d_1 = 0.57 \mu\text{m}$ as a function of the polar angle. 91

Figure 5.1. Schematic diagram showing the fabrication steps for the templates with the wrinkled patterns of the RM: (a) RMs on an alignment layer with one rubbing direction (R), (b) anisotropic one-directional wrinkled patterns by oxygen plasma treatment together with the wrinkle geometry, (c) RMs on an alignment layer with two rubbing directions (R_1 and R_2), and (d) anisotropic two directional wrinkled patterns by oxygen plasma treatment. The height and the period of the wrinkle are represented by h and λ , respectively. 96

Figure 5.2. (a)-(c) The microscopic images of regular one-directional wrinkle patterns prepared by several conditions of spin-coating rate: (a) 5500 rpm for 30 s, (b) 3500 rpm for 30 s, and (c) 1500

rpm for 30s. (d) The AFM image of a few wrinkled patterns of the RM. The inset shows the surface profiles of two patterns. (e) The wrinkle period (blue dashed line) and the wrinkle height (black dashed line) variations with the initial thickness of the RM film. 98

Figure 5.3. The microscopic images of LC texture aligned along two different directions being (a) perpendicular or (b) oblique to each other. The polarizer and the analyzer are denoted by P and A100

Figure 5.4. The SEM images of single line or multiple lines of colloidal microwires on (a)-(e) the one-directional wrinkled template or (f) the two-directional wrinkled template: (a) $r = 1 \mu\text{m}$, $\lambda \sim 4 \mu\text{m}$ (single line), (b) $r = 1 \mu\text{m}$, $\lambda \sim 5 \mu\text{m}$ (double lines), (c) $r = 1 \mu\text{m}$, $\lambda \sim 6 \mu\text{m}$ (triple lines), (d) $r = 2 \mu\text{m}$, $\lambda \sim 6 \mu\text{m}$ (single line), and (e) $r = 1 \mu\text{m}$, $\lambda \sim 7 \mu\text{m}$ (double lines), and (f) $r = 1 \mu\text{m}$, $\lambda \sim 4 \mu\text{m}$ (single line). Here, black arrow and dashed arrow represent the wrinkle direction and the slit-coating direction, respectively.102

List of Tables

Table 2.1. The information of the base material for the chiral nematic LC mixtures.	25
Table 3.1. Stokes vectors for common states of polarization.	51
Table 3.2. Mueller matrices for common optical elements.	53

Chapter 1

Introduction

1.1 Liquid Crystals

Liquid Crystal (LC) is a mesomorphic state which is intermediate between a crystalline solid and an amorphous liquid [1], or simply means a matter in such state. It has a directional order like a crystalline solid as well as some degree of fluidity like a liquid. Today, a large number of organic compounds are known to form the LC. Generally, LCs are categorized into three types by the mechanism for the phase transition: thermotropic, lyotropic, and metallotropic. Thermotropic LCs exhibit a phase transition into the liquid crystal phase as temperature is changed. Lyotropic LCs exhibit phase transition depending on both the temperature and the concentration of the LCs in a solvent. Metallotropic LCs are composed of both organic and inorganic molecules and their phase transition depends not only on the

temperature and the concentration, but also on the composition ratio of inorganic-organic molecules.

Since LCs have a certain order of molecular arrangement, they exhibit strong electrical and optical anisotropy which is not observed in other fluids. For instance, LCs change their orientation according to the direction of the applied electric field. The optical anisotropy of LC can be described by two local axes (long and short). Those local axes yield the different optical pathway between the polarization components along each axis. In general, sandwich-type cells consisting of two glass substrates deposited with an alignment layer and LCs between them are provided for examining the intrinsic properties of the LCs. In those LC cells, the alignment of the LC is governed by physical and chemical effects of the alignment layers so that the LC has the preferred orientations. The LC can be re-oriented by the external electric field applied across the substrates. The reorientation of LC gives a change in the optical properties of the LC cell. This is the basic operation principle of practical LC devices. Due to the large optical anisotropy and simplicity in electrical tuning capability, LCs have been widely used and studied in numerous fields.

The various LC phases (mesophases) can be characterized by the type of ordering. LCs can have two types of order: orientational order and positional order. Moreover, such orders can exist in either short-range or long-range. Most thermotropic LCs have an isotropic phase at high temperature. It means that the LC phase will be diminished by heating and eventually it changes into an isotropic phase at the temperature over clearing point. Under the lower temperature, the crystallinity of LC become more strong so that the one or more LC phase can be observed with an anisotropic orientation of molecules.

Most of thermotropic LCs consist of rod-like molecules and they are categorized into several phases according to their orientational or positional order. Several LC phases are described in Fig. 1.1.

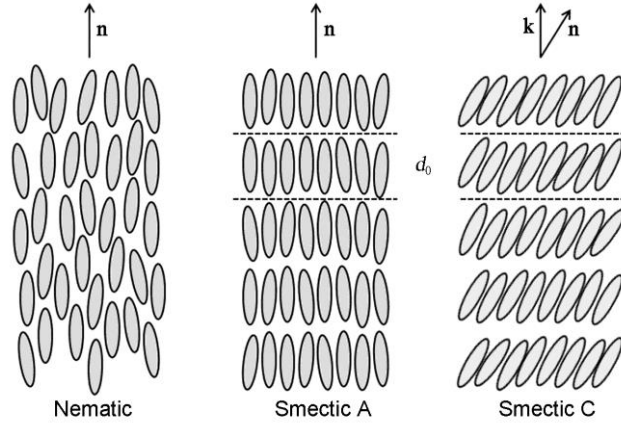


Figure 1.1. Schematic illustration of nematic (N), smectic A (SmA), and smectic C (SmC) phases.

Nematic phase

Nematic (N) phase possesses an orientational order, but no positional order in a long range. It means that the molecular centers of mass are randomly distributed throughout the medium. In N phase, the long axes of molecules are aligned on average to a particular direction. Therefore, N phase is optically uniaxial. The average direction of LC is often called as director and it can be indicated by a global vector \mathbf{n} . The degree of order in N phase is given by the order parameter S [2, 3],

$$S = \left\langle \frac{3}{2} \cos^2 \omega - \frac{1}{2} \right\rangle \quad (1.1)$$

where ω is the deviation angle of individual molecules from the director. Isotropic liquids have $S = 0$ and crystalline solids with a perfect orientational order have $S = 1$. LCs in N phase typically have $0.5 < S < 0.7$. The order parameter of the LC decreases as the temperature increases.

by lowering the temperature, additional features of order such as positional order can appear. This leads to the layered structures which are in fact regarded as two dimensional liquids.

Smectic A phase

In the smectic A (SmA) phase, molecules are oriented more or less parallel to each other and their position is ordered in layers. The layer spacing is approximately equal to the length of the molecules. Thus, SmA has orientational order as well as a degree of positional order described by smectic layers. The director in SmA phase is normal to the smectic layers and corresponds to the optic axis of the system. In reality, however, the smectic layers are not strictly defined, but a plot of the density of centers of mass versus distance along an axis parallel to the director, which follows a sinusoidal variation:

$$\rho_s(x) = \rho_o \left\{ 1 + \psi \sin \left(\frac{2\pi z}{d_0} \right) \right\} \quad (1.2)$$

where ρ_o , d_0 , and ψ are the mean density, the spacing of smectic layer (typically a few nanometers), and the smectic order parameter [4], respectively. Here, the

smectic order parameter is the ratio of the oscillation amplitude to the mean density of smectic layer. LC molecules are able to diffuse within a layer but there is no positional correlation between the molecules in different layers. The smectic layers can be easily distorted but the spacing between the layers tends to be preserved. The SmA phase, similarly to the N phase, is optically uniaxial.

Smectic C phase

The molecules in the Smectic C phase (SmC) are arranged in layers like SmA phase but they are not free to rotate around their long axis. In SmC phase, the molecules are aligned along a tilted direction with respect to the normal axis of the smectic layer. The tilted direction in neighbouring layer is identical to each other so that the projections of the molecules to the plane of the layers are aligned in a common direction. Since the tilt is uniform over the whole structure, the arrangement is alternatively called as synclonic order. The projected director of the molecules is denoted by a unit vector \mathbf{c} . The tilt angle of molecules can be defined as the angle between the director of molecules (\mathbf{k}) and the normal axis of the smectic layer (\mathbf{n}) and the plane spanned by \mathbf{k} and \mathbf{n} is usually called as tilt plane. The variance of \mathbf{k} out of the conical surface obtained by the rotation of \mathbf{k} about \mathbf{n} is strictly prohibited. The SmC phase is optically biaxial because there is no rotational symmetry about \mathbf{k} .

Various LCs, especially mixtures, usually have more than one LC phase. Typically, the sequence of phases appearing from low temperature to high temperature follows crystal – SmC – SmA – N – isotropic phase. The LC phases observed at lower temperature are more ordered phases than that at higher temperature.

Chiral nematic phase

When chiral molecules (chiral dopant) are mixed with LCs in N phase, chiral nematic (N^*) phase with twisted structure is formed. The director in N^* phase rotates about an axis perpendicular to the director plane as shown in Fig. 1.2. As a result, the helical superstructure is macroscopically formed. It is called as helix. In helix, the distance made by one rotation of director (2π radians) along the helix axis is called as helical pitch, p . The pitch strongly depends on the concentration of the chiral dopant and varies typically between a few hundred nanometers to many micrometers. Due to $\mathbf{n} = -\mathbf{n}$ symmetry of the N^* phase, the periodicity is given by half of the helical pitch. The chiral twist can be either right- or left-handed, depending on the configuration of chiral elements within the molecule. In some N^* phase, the pitch is similar to the wavelength of visible light. It leads to Bragg reflection of visible light which is circularly polarized in same handedness of the twist.

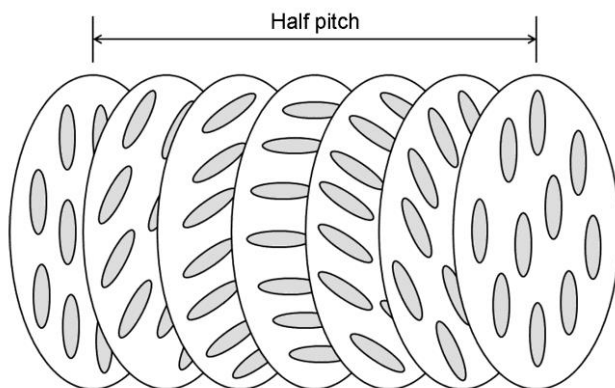


Figure 1.2. Schematic illustration of the chiral nematic (N^*) phase.

Chiral smectic phases

When chiral molecules are mixed with LCs in SmC phase, the ferroelectric or helielectric (SmC*) phase is formed. SmC* phase has a helicoidal superstructure which is similarly characterized by helical pitch and its sign. As shown in Fig. 1.3, the tilted director rotates about the helical axis drawing conical surface progressively from layer to layer with a preserved azimuthal angle in single layer. This phase SmC* phase exhibit a local spontaneous polarization \mathbf{P}_s laying on the smectic layer plane which is perpendicular to the plane spanned by \mathbf{k} and \mathbf{n} (tilt plane). The magnitude of the polarization as well as the magnitude and the sign of the helical pitch can be varied by modifying the mixing ratio between SmC* compounds.

In an undistorted field-free SmC* phase, the average of spontaneous polarization over one pitch is zero. It results in no macroscopic polarization of the system. In this case, the helielectric state is more appropriate for description than ferroelectric state. Application of an electric field along the perpendicular direction of the helix axis will couple the polarization vector. It unwinds the helix and \mathbf{P}_s is reoriented according to the direction of the applied field. In addition, the helix also can be unwound by surface actions. This state exhibits ferroelectric properties. Such configuration is called as surface stabilized ferroelectric liquid crystal (SSFLC).

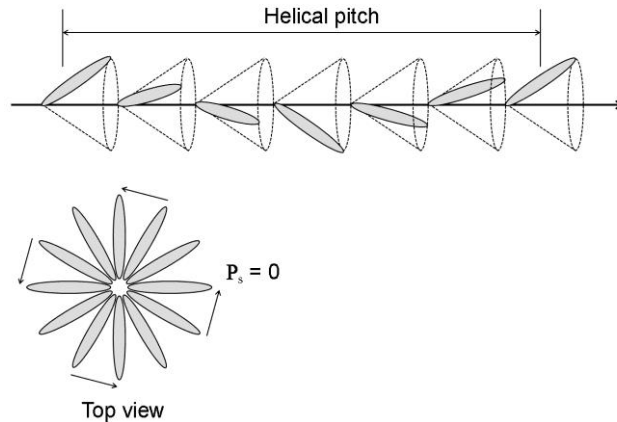


Figure 1.3. Schematic illustration of the chiral smectic (SmC*) phase.

Other phases

Since both SmA and SmC phases have no positional order within each layer, they can be considered as the layered system ordered in one dimension. However, the molecules are often ordered within the layer in other smectic phases. The order within the layer is called as bond orientational order. In hexatic phase, the molecular centers of mass within a layer are arranged in oriented hexagonal manner. This phase is then ordered in three dimension. A number of arrangements have been reported such as SmB (no tilt within layers), SmI (molecules tilted towards apex of the hexagon) and SmF (molecules tilted towards side of the hexagon) [2].

1.2 Reactive Mesogens

Mesogen refers to a material that exhibiting LC properties and mesogenic is the term given to a substance that induces LC phase. The mesogenic materials are composed of rigid and flexible parts, which characterize the order and the mobility. The rigid segments enable to align the mesogen in one direction and have distinctive shapes that are typically found in the form of rod or disk shapes. The flexible segments provide mesogens with mobility because they are usually made up of alkyl chains which hinder crystallization to a certain degree. The combination of rigid and flexible chains induces structural alignment and fluidity.

The reactive mesogens (RMs) are the chemical compounds exhibiting LC properties as well as being capable of the polymerization. In general, RMs has low molecular mass similar to LCs with polymerizable groups at tails. The polymerization occurs via a number of reaction mechanisms that vary in complexity due to functional groups in reacting compounds [5] and their inherent steric effects. In more straightforward polymerization, alkenes, which are relatively stable due to sigma bonding between carbon atoms, form polymers through relatively simple radical reactions. In contrast, more complex reactions such as those that involve substitution at the carbonyl group require more complicated synthesis due to the way in which reacting molecules polymerize [5]. The schematic diagram showing the cross-linking process of the RMs is shown in Fig. 1.4. By the cross-linking process with the help of external energy such as heat and the exposure of light, RMs forms the liquid crystalline polymer (LCP). Typically, LCPs have a high mechanical strength at high temperatures, extreme chemical resistance, inherent flame retardancy, and good weatherability. The molecular structure of RM is designed to have the ability of combining various functional groups and fragments, as well as the ability of polymerization to form stable films,

fibres, and coatings that can be applied onto various substrates. In usual, the commercially available RMs have mono-acrylate or di-acrylate tails helping the photo-polymerization and the polymerized RMs becomes extremely unreactive and inert. They exhibit LC phase at low temperature and by the photo-polymerization process the phase is permanently fixed if the LC cores are aligned in the ordered manner by the aligning treatment on target surface.

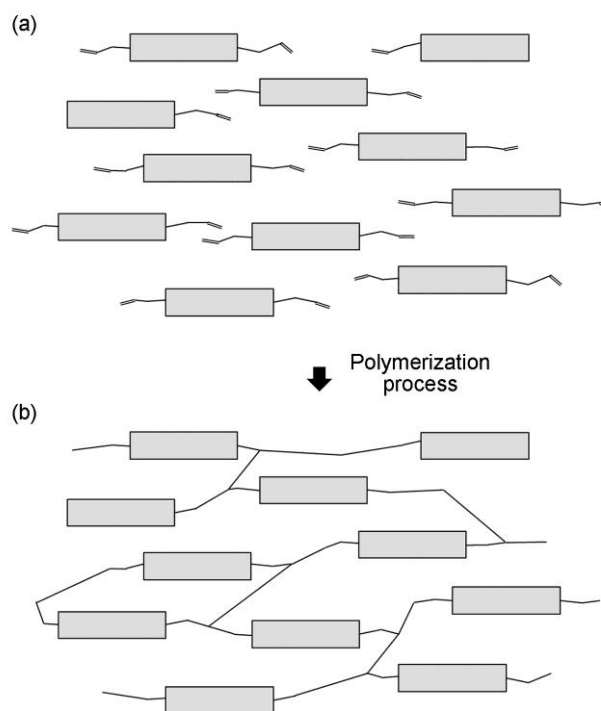


Figure 1.4. Schematic illustration of (a) the RM and (b) the LCP formed by the polymerization of the RM.

The RMs are often dissolved in a solvent to producing a stable LCP film by simple methods such as spin coating, dipping, lamination, etc. The RM films are

produced by the deposition of the solvent on the alignment layer with pre-defined aligning direction and the photo-polymerization process by the exposure of ultraviolet (UV) light. Depending on the materials and the aligning condition, several LC phase such as N phase (both in horizontal and vertical direction) and N* phase can be formed in the polymerized layer. However, the degree of order is somewhat less than that of a regular solid crystal.

When RMs are mixed into usual LCs, the RMs obtain the order in molecular direction identically to the phase of host LC. The polymerization of LC/RM mixture leads to a bicontinuous phase separation between the polymerized RM and the LC. It forms a LC/RM composite system where the polymer matrix is capable of stabilizing the phase of host LC in wide range of temperature or inducing the phase of host LC to the newly dispersed LC in it. This is called as a polymer-stabilized LC and a polymer-dispersed LC, respectively. The LC/RM composite systems have been widely studied in the areas of LC technology for the various applications such as electro-optical devices, and displays.

1.3 Outline of Thesis

This thesis contains six chapters. In Chapter 1, several examples of the LC phase and the basics of RMs together with the LC/RM composite system are introduced.

In Chapter 2, the aligning capability of the RM is discussed. At first, LC/RM composite systems were constructed by the formation of patterns of polymerized

RM on the bottom substrate of LC cell. In both case of the horizontal and the vertical alignment of LC, the highly uniform alignment of LC across the RM patterns was achieved by the anisotropic directional preference of RM. This uniform alignment was hindered in the LC/isotropic polymer composite system where the polymer patterns constructed through the transfer printing of fluorinated polymer, owing to the monotonic directional preference of the isotropic polymer. Second, the polymer-stabilization of LC induced by the photo-polymerization of RM initialized from the alignment surface. In contrast with previous approaches, the photo-polymerization selectively initialized from alignment surface forms the discrete parts of pure LC region and the LC/RM composite region in the separated configuration. Here, the chiral LC mixture composed of RM, chiral dopant, and LC in various concentration ratios was prepared for studying the growth of polymer matrix and the optical spectrum depending on the density of RM. In the end of this chapter, the self-organization of surface structure induced by the buckling instability of the RM film is described. The polymerization of RM film was carried out by the vacuum plasma treatment of which energy hardly penetrate the bulk of RM film, so that the depth-wise gradual polymerization was achieved. During the plasma treatment, the RM film thermally swells. After cooling of RM film, the buckling instability between the polymerized region and soft region induces the nano-to-micro topography such as nanobumps and wrinkles on surface. In addition, the initial alignment of RM induced the uniform wrinkles aligned along the direction of RM molecules. The conditions of the polymerization are differed in a several way and the corresponding surface topography was experimentally demonstrated.

In Chapter 3, the reflective liquid crystal display (RLCD) based on the

polarization selective reflector (PSR) of chiral reactive mesogen (CRM) is described. The RLCD consists of the PSR on the bottom substrate and the horizontally aligned bulk LC on the PSR. The bulk LC acts as a role of a tunable phase retarder for the incident polarized light depending on the applied voltage. In front of the PSR, only the circularly polarized component of light in certain wavelength similar with the helical pitch of PSR is reflected. Compared to the previous research where the color filter is placed in front of the cell and mirror is on the bottom of the cell, the PSR combined two functionalities from both components so that the reflectance and color purity is greatly improved. The electro-optical property of the RLCD based on the PSR was examined both in a theoretical and experimental way. In end of this chapter, the prototype RLCD integrated with three types of PSR for the reflection of three primary colors was demonstrated.

In Chapter 4, a new type of LCD based on the anisotropic voltage-dividing layer (AVDL) of RMs for reducing the gamma distortion is demonstrated. The AVDL acts as a role of capacitance for shifting the threshold voltage in sub-domain and is capable of spontaneously aligning the LC molecules without any planarization process. The threshold difference compensates the difference of the phase retardation between the normal and an oblique viewing direction, which results in the reduction of the gamma distortions. The alignment property of LC across the AVDL depending on the UV exposure time for the photo-polymerization of the RM is examined. Both the numerical simulations and the experimental measurement for the assessment of the gamma distortion were performed in the patterned vertical alignment (PVA) mode.

In Chapter 5, a novel concept of a directional colloidal assembly by using

wrinkle pattern on the aligned RM surface is introduced. The periodic wrinkle pattern is organized from the bi-layer configuration of RM film where the weakly polymerized layer is remained under the heavily polymerized thin surface layer. The periodic wrinkle pattern on the RM surface plays a role as a template for the directional assembly of the polystyrene (PS) colloidal particles. The periodicity of wrinkle pattern is determined according to the thickness of RM film and UV exposure time. The single line or multiple lines of directional colloidal assembly are produced by varying the period of wrinkles and the size of the PS particle.

Finally, the summary and some concluding remarks are made in Chapter 6.

Chapter 2

Aligning Capability of Reactive Mesogens

2.1 Introduction

The polymerization of RMs forms the LCP which has a certain degree of LC phase in a solid state. The aligning capability of RMs is primarily originated from the intrinsic anisotropic natures of RMs similar to the LC. The polymerized RM with an order in the molecular direction makes surface characteristics to be varied according to the direction of the RM. Thus, the surface characteristics of RM film depend on the initial alignment state of RM. This is unique property compared with the usual polymerized structure where the surface characteristic is monotonic, and the spatial variance is hardly observed due to their isotropic nature. In this chapter,

the LC aligning capability of RM in the several LC/RM composite systems will be discussed. Since the RM is similar with the LC in shape, dimension, and molecular weight, such variance in surface characteristics of the RM structure will produce strong unusual interaction compared with the other polymer structure. In addition, the self-organization of the surface topography on RM film induced by the alignment of the RM will be introduced. In the aligned RM structure, the elastic constant is anisotropic so that the direction of the surface topography can be defined during the relief process of the buckling instability. Such ordered topographies have been observed only from the mechanical stretching of the elastomer in bi-layer configuration. A number of the self-organized surface topography in nano-to-micro range will be demonstrated with the basic principle of the buckling instability.

2.2 Liquid Crystal/Reactive Mesogen Composite Systems

2.2.1 Liquid crystals on patterned reactive mesogen film

Usually, the un-planar boundary condition such as protrusion induces the tilt change of LCs. It is mainly due to the monotonic directional preference of the surface structure. At interface between LC and RM, the interaction occurs in different manner. Here, aligning capability of the patterns of the RM film formed on the bottom substrate of LC cell will be studied.

Horizontally aligned system

Figure 2.1 shows the fabrication process of LC cell with the RM patterns on the bottom substrate. For uniform alignment of the RMs and LCs, a homogeneous alignment material AL22620 (JSR Co.) was spin-coated at the rate of 3000 rpm for 30 s on the bottom glass substrate and thermally annealed at 180°C for 1 h. The surface of the alignment layer was subsequently rubbed by a conventional roller type rubbing machine. A mixture of the RMs and the photo-initiator in propylene glycol monomethyl ether acetate (PGMEA) solution (RMS03-013C, Merck) was then spin-coated at the rate of 3000 rpms for 30 s on the alignment layer and softly annealed at 75°C for 60 s to remove the solvent. The RM layer was photo-polymerized with the photomask under the UV at the intensity of 20 mW/cm² for 120 s. The un-polymerized RMs were removed by PGMEA (Sigma Aldrich Korea) and fully dried at 75 °C. The cells with the 5 μm cell gaps were constructed and the positive LC, ZLI-5400-075 ($n_e = 1.6549$, $\Delta n = 0.1544$, Merck) was infiltrated by the capillary action. Note that the upper glass substrate was prepared by the deposition of alignment layer in same method as described above and rubbed in the anti-parallel direction of the bottom substrate.

Vertically aligned system

A homeotropic alignment material (AL60702, JSR Co.) was spin-coated at the rate of 3000 rpm for 30 s on the two glass substrates and post-annealed at 150°C for 1 h. A mixture of RMs and the photo-initiator in p-xylene solution (RMS03-015, Merck) was spin-coated at the rate of 3000 rpms for 30 s on the alignment layer and softly annealed 75°C for 60 s. It should be emphasized that the RMs in RMS03-015 enables to align itself in vertical direction on the homeotropic

alignment layer by a simple spin-coting process. The RM layer was photo-polymerized with the help of the photomask by the exposure of UV at the intensity of 20 mW/cm^2 for 120 s. The remained RMs were washed out by p-xylene (Sigma Aldrich Korea) and fully dried at 75°C . The cells with the $5 \mu\text{m}$ cell gaps were constructed and the LC, ZLI-5400-075 was infiltrated by the capillary action. Figure 2.1 shows the schematic diagram of the fabrication process.

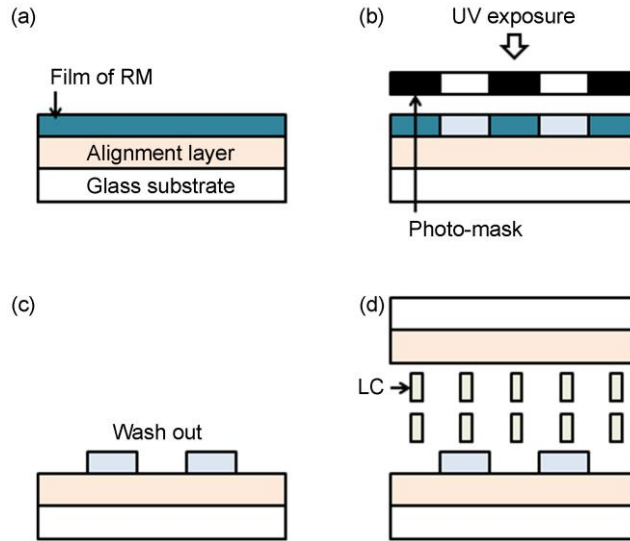


Figure 2.1. Fabrication process of LC cell with the RM patterns on the bottom substrate. (a) Spin-coating of the RM on the alignment layer. (b) Photo-polymerization process with the photomask. (c) Wash out process for the removal of un-polymerized RM. (d) Construction of the cell and the infiltration of LC.

Patterning of the isotropic polymer

For the comparison, the patterned layer of fluorinated polymer, EGC-1700 (3M Novec) was prepared by substitution of vertically aligned RM, RMS03-015. The surface of EGC-1700 is dominated by mainly CF_3 groups which enable to effectively reduce the surface tension by lowering the density of the attractive centers per unit area at the surface. The uniformly organized CF_3 groups are capable of providing the surface with the surface tension as low as 6 mN/m^2 so that the LC is vertically aligned on the surface. The fluorinated polymer solution was prepared by dissolving EGC-1700 in HFE-7100 (3M Novec) with the concentration of 2 wt.%. HFE-7100 is a highly fluoruous-solvents which guarantees the chemical compatibility of EGC-1700. In addition, HFE-7100 can be deposited easily on various surfaces including a glass, a metal foil, and even polymer surface regardless of the surface characteristics since it has the very low boiling point (61°C). Thus, a uniform film of EGC-1700 of which thickness is in range from a few tens of nanometers to a hundreds of nanometers can be provided by dip-coating or spin-coating technique. The fluoruous polymer solution was deposited on the surface of an elastomeric stamp of poly(dimethylsiloxane) (PDMS) having line and space patterns. The patterns of fluoruous polymer were then produced by transfer-printing process onto the homeotropic alignment layer as shown in the Fig. 2.2(b). For this process, the work of adhesion between the mold and polymer interface W_{mp} should be smaller than that between the polymer and substrate interface W_{ps} . Here, the work of adhesion can be described as

$$W_{\text{mp}} - W_{\text{pa}} = (\gamma_{\text{a}} - \gamma_{\text{m}}) - (\gamma_{\text{pa}} - \gamma_{\text{mp}}), \quad (2.1)$$

where γ_m , γ_p , and γ_a denote the surface energy of the mold, the fluorinated polymer, and the alignment layer, respectively, and γ_{pa} and γ_{mp} denote the interfacial binding energy between the fluorinated polymer and the alignment layer and that between the mold and the fluorinated polymer, respectively. The difference between two work of adhesion ($W_{mp} - W_{ps}$) is approximately equal to the surface energy difference between the alignment layer and the mold ($\gamma_a - \gamma_m$), because the term $\gamma_{pa} - \gamma_{mp}$ is negligibly small. In this experiment, accordingly, the fluorous polymer solution on PDMS was transferred onto the alignment by the low adhesion of the PDMS compared to that of the glass substrate. After that, the LC cell was identically constructed as shown in Fig. 2.2.

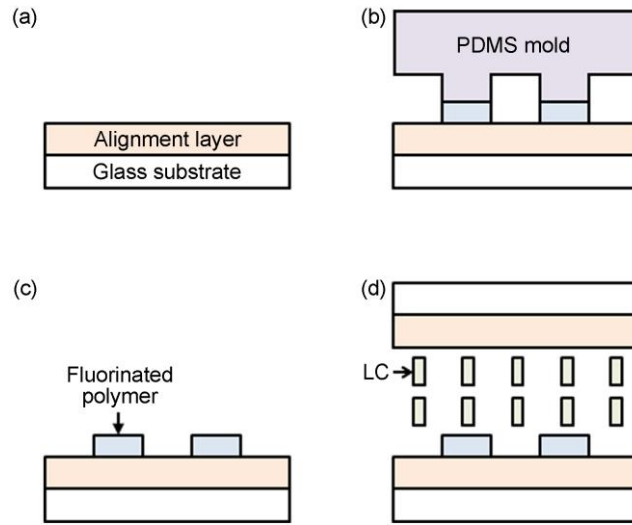


Figure 2.2. Fabrication process of LC cell with the isotropic patterns on the bottom substrate. (a) Spin-coating of alignment layer on the glass substrate. (b) Contact of PDMS mold deposited with fluorinated polymer on the alignment layer. (c) Transfer-printed fluorinated

polymer patterns. (d) Construction of the cell and the infiltration of LC.

Results and discussion

Figure 2.3 shows the microscopic images of the fabricated LC cells. The lines and spaces pattern of RMs were well defined as shown in Figs. 2.3(a) and 2.3(c). The microscopic image under the cross polarizer (*A*: analyzer, *P*: polarizer) as can be seen in Figs. 2.3(b) and 2.3(d), highly uniform alignment of LC molecules was observed across the RMs patterns. In conventional case, however, the patterns constructed using isotropic material can induce alignment distortion across the patterns.

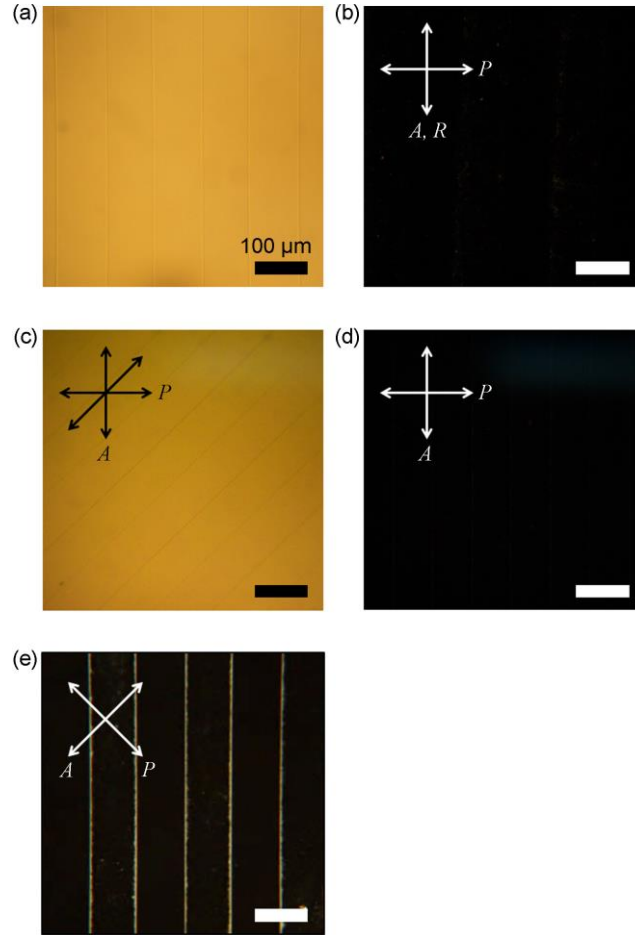


Figure 2.3. (a)-(d) Microscopic images of LC cell with the RM patterns on the bottom substrate. (a), (b) Horizontally aligned LC cell. Here, A , P , and R denote the analyzer, the polarizer, and the rubbing direction, respectively. (c), (d) Vertically aligned LC cell. (e) Microscopic images of vertically aligned LC cell with the fluorinated polymer patterns on the bottom substrate.

As an example of the conventional case, Fig. 2.3(e) shows the microscopic

texture of the LC cell with patterned fluorinated polymer on bottom substrate. It is clearly observed that light leakage occurred in the several line regions which correspond to the edge of the polymer patterns. It means that the directional preference of the LC molecule on the surface of the isotropic patterns is monotonic. In such configuration, the direction of the LC alignment is varied at each surface of pattern of which the normal axis differs to each other (e.g. lateral direction by the wall of pattern and upper direction by the surface of pattern). Therefore, such monotonic directional preference of surfaces results in the alignment collision and light leakage from it. On the other hand, the patterns of RMs have anisotropic directional preference due to the RM's inherent anisotropy in molecular shape and its arrangement. Thus, the highly uniform alignment of LC can be achieved regardless of the pattern shape and its thickness unless the order of RMs is broken. The conceptual diagram for the comparison between the LC alignment on the isotropic patterns and the anisotropic patterns is depicted in Fig. 2.4.

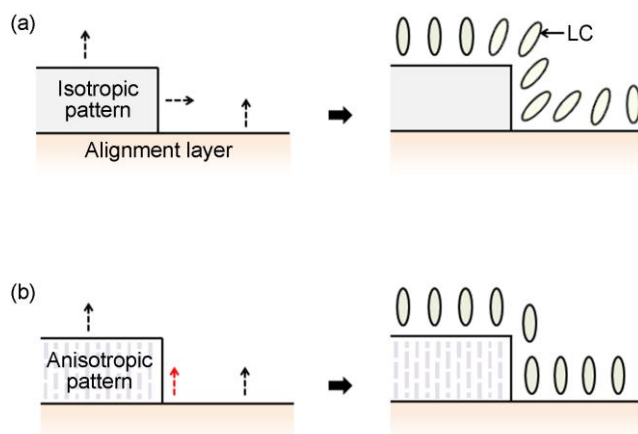


Figure 2.4. Schematic diagram of the directional preference of LC

and the resultant alignment of LC near (a) the isotropic pattern and (b) the anisotropic pattern.

2.2.2 Stabilization of liquid crystals by reactive mesogen

The polymer-stabilization of LC has drawn much attention in the electro-optical applications since it can improve the electro-optical property in the cost-effective way [6-10]. Usually polymer stabilization process was carried out by using the LC/RM mixture doped with the photo-initiator. After the polymerization process, the polymer matrix is spontaneously formed over the region exposed to the external energy. The photo-initiator can be doped in the alignment layer, instead of the LC/RM mixture. It can lead to the surface-initialized photo-polymerization of RM. Here, the surface-initialized polymer stabilization process using RM will be examined.

Four mixtures containing LC, RM, and chiral dopant at various ratio in wt.% were prepared. The mixture 1 (M_1) was composed of the negative LC, MJ981185 ($n_e = 1.5957$, $\Delta n = 0.1102$, Merck), the RM, RM257 (Merck), and the chiral dopant, R-811 (Merck) in the relative concentrations of 71.68 wt%, 10.43 wt%, and 17.89 wt%, respectively. The three other mixtures which are named mixture 2 (M_2), mixture 3 (M_3), and mixture 4 (M_4) were composed of the same material but in the different ratio. Table 2.1 shows the material information of the prepared mixture. Note that the concentration of the chiral dopant was kept in the range of 17% ~ 18% in the all mixtures for generating a red tone color equally, but the concentration of the RM is differed in mixture by mixture, maintaining the sum of

concentration of the LC and the RM in the range around 82% ~ 83%.

	M ₁	M ₂	M ₃	M ₄
LC (%)	71.68	62.78	51.75	40.81
RM (%)	10.43	20.15	30.06	41.62
Chiral dopant (%)	17.89	17.07	18.20	17.57

Table 2.1. The information of the base material for the chiral nematic LC mixtures.

Fabrication process

Figure 2.5 shows the fabrication process of the polymer stabilized LC cell based on the polymer network selectively formed on the bottom substrate. A homogeneous alignment material AL22620 doped with the 1 wt.% of photo-initiator (4-(dimethylamino)-benzophenone; Sigma Aldrich) was spin-coated at the rate of 3000 rpm for 30 s on the bottom glass substrate and annealed at 180°C for 1 h. The top glass substrate was deposited with the pure AL22620 and both surface of the alignment layer was rubbed in anti-parallel direction. The cell gap was maintained to be 10 μ m and the various mixtures described above was infiltrated by capillary actions at the temperature condition right below the clearing point of each mixture for preventing the phase separation between the base materials. Note

that the severe difference in molecular weight between base materials also results in the phase separation during the infiltration process due to the different propagation speed in the cell. The cell was exposed to UV at the intensity of 20mW/cm^2 for several different times through the photomask. Here, the bottom substrate with the doped alignment layer was made to face the photomask. The polymer network then grew at the bottom substrate by the help of photo-initiator doped in the bottom alignment layer. After the UV exposure, the remaining mixture in cell was fully removed in acetone for about 1 day. Finally, the cell was filled with the positive LC, ZLI-5400-075.

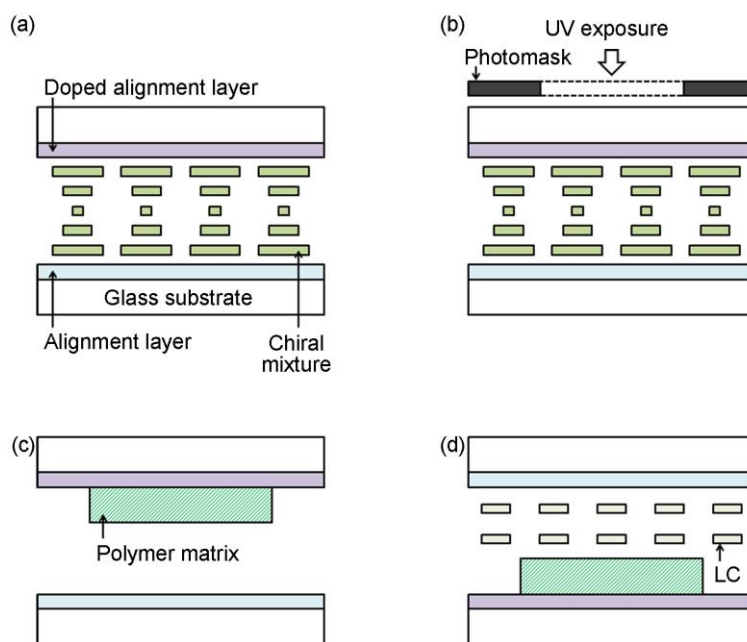


Figure 2.5. Schematic diagram showing the fabrication process of the polymer stabilized LC cell based on the polymer network. (a) Cell

filled with the chiral mixture. Here, one alignment layer was doped with the photo-initiator. (b) Photo-polymerization by the UV exposure. Bottom substrate faces the photomask (c) Wash out process for the removal of chiral mixture. (d) Infiltration of nematic LC.

Results and discussion

The scanning electron microscopy (SEM) images of the part of polymer networks formed on the bottom substrate using M_1 at the four conditions of the UV exposure times (20 s, 40 s, 60 s, and 80 s) are shown in Fig. 2.6. The network structures found to become clearer as the exposure time increases. In the cases of the 20 s and 40 s of UV exposure times as shown in Figs. 2.6(a) and (b), the insufficient polymer network with a lack of porosity was defined. At the longer UV exposure time over 40 s as can be seen in Figs. 2.6(c) and (d), the polymer network with the higher density of the porous region was formed so that it can act as an infiltrating medium for the LC molecules and is capable of inducing the memorized phase (chiral nematic phase in this experiment) to newly injected the LC.

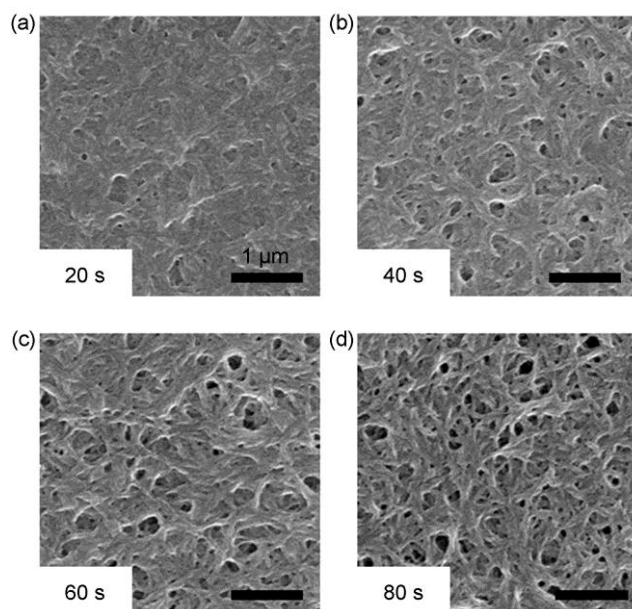


Figure 2.6. SEM images of the part of polymer networks formed on the bottom substrate using M_1 at the UV exposure times of (a) 20 s, (b) 40 s, (c) 60 s, and (d) 80 s.

Figure 2.7 shows the SEM images of the part of polymer networks formed on the bottom substrate using four mixtures (M_1 , M_2 , M_3 , and M_4) at the 80 s of UV exposure time. As mentioned above, the mixtures were differed in the concentration ratio of the RM while the concentration ratio of the chiral dopant was similar to each other. In the case of the higher density of RM, it is found that the size of pore decreased by the thicker frame of the polymer network. As a result, even the number of the porous region per unit area was still maintained, the density of the porous region decreased. It means that the color purity of the polymer stabilized LC will decrease since the density of the stabilized LC in chiral nematic

phase is small to exhibit Bragg reflection. In contrast, the phase memory effect of the polymer network will be diminished at the lower density of the RM. In other words, the newly infiltrated LC will have a lack of chirality where the only the optical property of N phase is observed. Thus, the proper concentration of the RM should be chosen for generating the phase memory effect as well as exhibiting vivid color. In this experiment, the optimized concentration of RM was experimentally found to be in range of 20% ~ 25%.

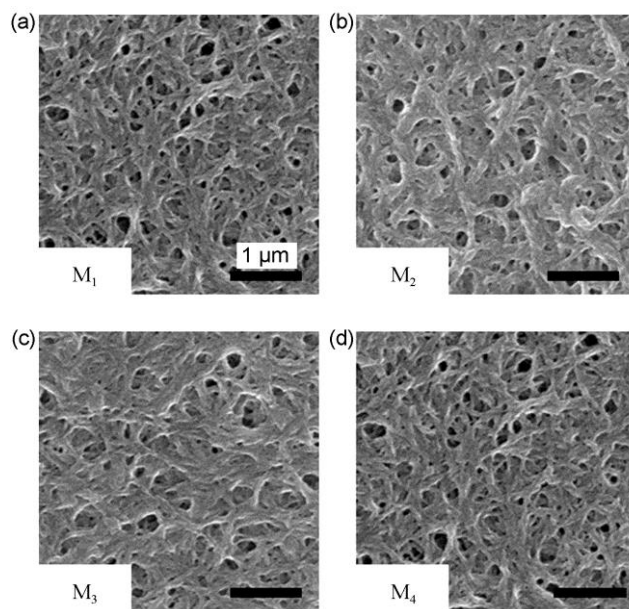


Figure 2.7. SEM images of the part of polymer networks formed on the bottom substrate using (a) M₁, (a) M₂, (a) M₃, and (a) M₄ at the 80 s of the UV exposure times.

Figure 2.8 shows the thickness of the polymer network produced from four

mixtures as a function of UV exposure time. The thickness of the polymer network becomes thicker as the concentration of the RM and the UV exposure time increase. The thickness was then saturated at the certain value as a function of the UV exposure time. It is due to the surface initiation of the photo-polymerization where the photo-initiator in surface is hardly diffused into bulk of cell. The saturation value is determined by the concentration of RM. It means that the saturation value increases as the concentration of the RM increases. The relationship between the saturation of thickness and the concentration of the RM might be valid until the certain value of the concentration over which the ratio of the photo-initiator compared to the RM is too small to increase further the thickness of the polymer network. This assumption can be experimentally examined by extremely lowering the doping ratio of the photo-initiator in the alignment layer.

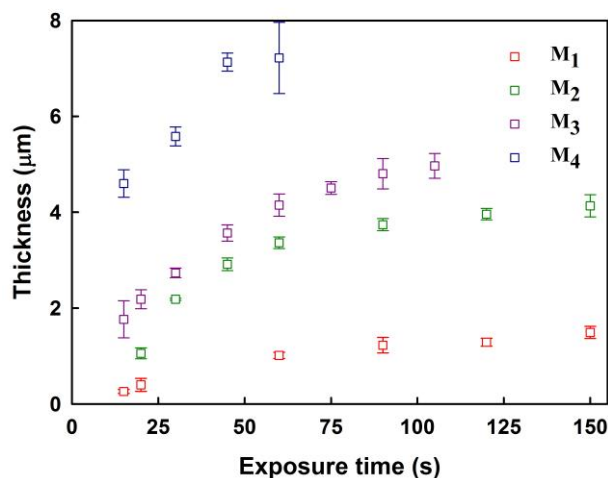


Figure 2.8. Thickness of the polymer network produced from four mixtures as a function of UV exposure time.

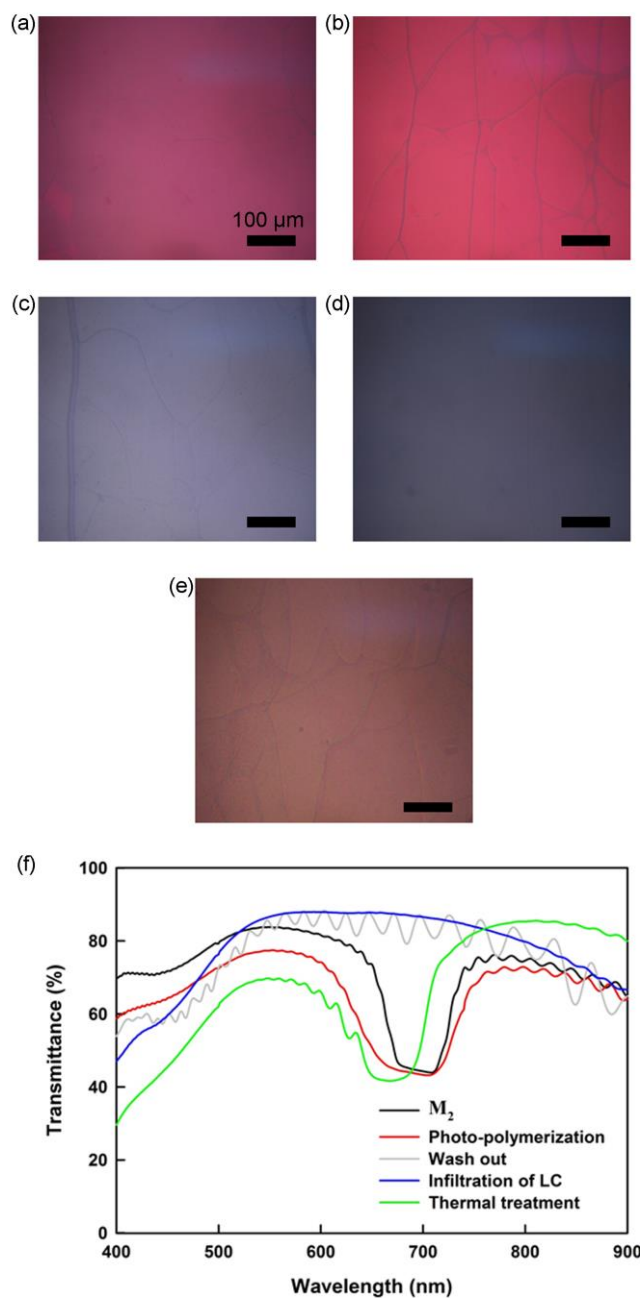


Figure 2.9. Microscopic images of the sample cell at each fabrication step using M_2 . (a) The initial state filled with the M_2 . (b) The photo-

polymerization process. (c) The wash out process. (d) The re-infiltration of LC. (e) The thermal treatment. (f) The optical spectra of the corresponding state shown in (a) ~ (e).

Figure 2.9 shows the several optical spectra of the cell under the certain point of the fabrication process. Here, M_2 were used for this experiment. The black line represents the spectrum of the cell filled with the mixture before the photo-polymerization. This spectrum corresponds to the photonic bandgap structure of the chiral nematic phase with the forbidden bandwidth around 700 ± 10 nm. The spectrum after the photo-polymerization (red line) was similar with that before the photo-polymerization, but the band was broadened. It is mainly due to the formation of the gradient helical pitch by the diffusion of the RM [11]. This phenomenon is more predominant in case of the higher concentration of the RM. Also, the chiral pitch can be thermally extended during the photo-polymerization process [12]. After the wash out process, the bandwidth disappeared. It can be inferred therefore that the polymer network itself is unable to exhibit Bragg reflection even the RM is aligned in chiral phase. Interestingly, a similar result was still observed right after the infiltration of LC (blue line in Fig. 2.9). It means that the external condition such as the temperature is required to the infiltration of LC into the polymer matrix, which is clearly confirmed by the optical bandwidth of thermally treated sample (green line in Fig. 2.9). Note that the band shift of the thermally treated sample from the initial condition is mainly owing to the difference in the refractive index of the host LC (MJ981185) and the infiltrated LC (ZLI-5400-075). The optical spectra of the cell constructed using M_4 is also shown in Fig. 2.10.

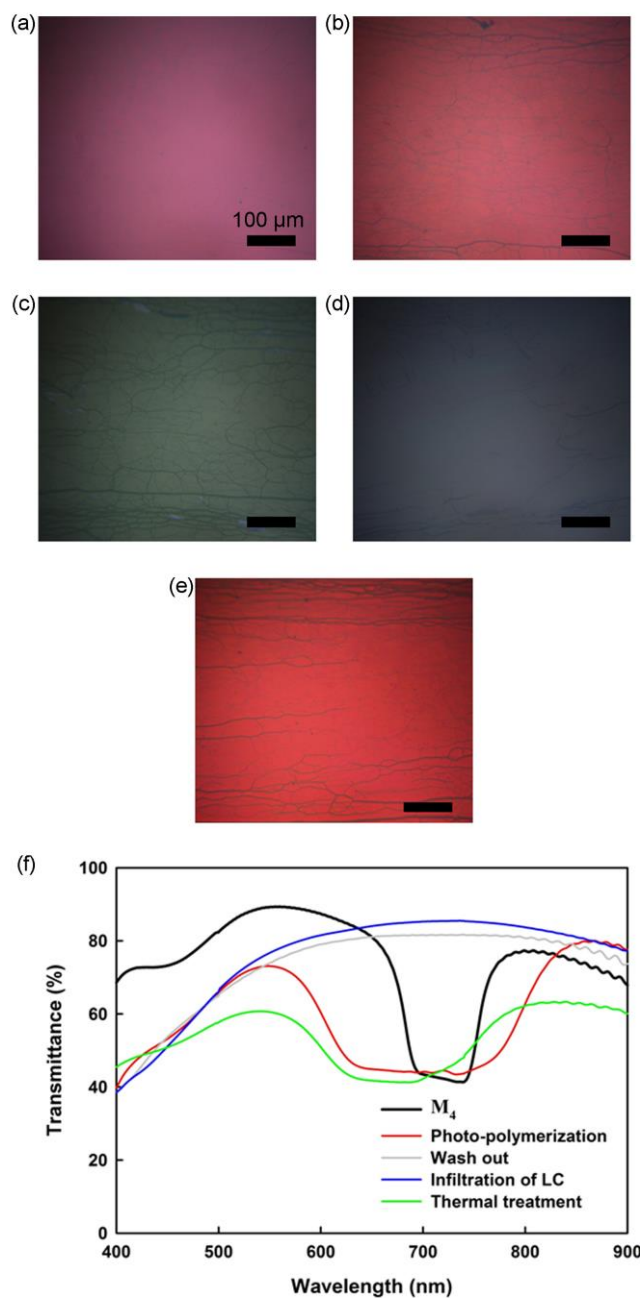


Figure 2.10. Microscopic images of the sample cell at each fabrication step using M_4 . (a) The initial state filled with the M_4 . (b)

The photo-polymerization process. (c) The wash out process. (d) The re-infiltration of LC. (e) The thermal treatment. (f) The optical spectra of the corresponding state shown in (a) ~ (e).

2.4 Self-Organized Surface Topography of Reactive Mesogen

Until quite recently, the surface topography is produced by a pre-straining and releasing process of the bilayer elastic films which undergo a buckling instability from the mismatch in the equilibrium state between the stacked layers. The buckling instability leads to the stress relaxation process and the surface topography is formed as a consequence.

In the polymerization process of the monomer films, the surface uniformity is primarily determined by the intensity and/or the exposure time of the external energy. During the photo-polymerization process, for example, the monomer diffuses to adjacent vacancy. This diffusion process is governed by the concentration of the monomer and that of the polymer. The concentrations of monomer and polymer are the function of the exposure time and energy [13]. Usually, the density of the light and exposure time for the uniform surface is in low range where the parameters relating to the monomer diffusion can be spatially uniform. On the contrary, the higher energy density can yield the concentration of the polymers differed in lateral direction. It leads to a depth-wise gradient of the polymerization. This state can be considered as the layer in the gradation where the

surface topography similarly formed by the stress relaxation process. In addition, the remnant heat from the light enables to induce more the gradation in the system (thermal expansion).

The plasma treatment is used for treating a surface with the higher energy density compared to the UV light. It is also capable of providing the non-uniformity on the surface because the energy penetration hardly occurs through the bulk of the system. Thus, the gradient of the polymerization becomes more distinguishable. The surface topography of monomer film through the plasma treatment is shown in Fig. 2.11. Note that the temperature of plasma atmosphere is raised up to 100 °C during the vacuum plasma treatment so that the thermal swelling of the monomer film is induced. The pre-cured hard layer is first formed at the surface of the swelled monomer film. After the plasma treatment, the cooling of the monomer film generates buckling instability between the fully cured top region and the softly cured bottom region. As a consequence, the surface topography is formed.

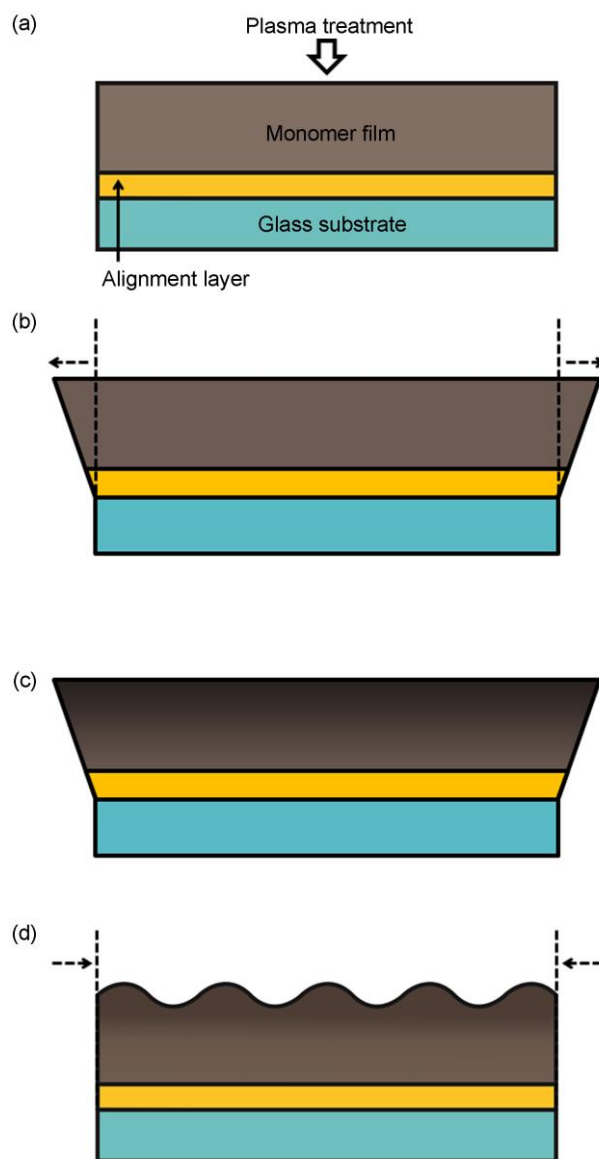


Figure 2.11. Schematic diagram showing the surface topography of the monomer film. (a) Plasma treatment on the surface of the monomer film. (b) The thermal swelling of the monomer film. (c) The depth-wise gradient polymerization. (d) The surface topography

induced by the buckling instability after the cooling of the monomer film.

Polymerization of RM by plasma treatment

The RM, unlike usual monomer, has the anisotropic property originated from the body shape and it gives a certain degree of order on the polymerized film. When the plasma treatment is applied to the aligned RM film, the thermal strain shows an anisotropic property. This anisotropic property yields the uniform wrinkled patterns. Note that the previous elastomer-based approach mechanically gives a strain by the machine. The anisotropy in RM, on the other hands, is simply given by aligning of the RM on the usual alignment layer. In addition, the spatial variance of aligning direction in alignment layer can be induced by a number of multi-directional alignment techniques. It results in the surface topography in multiple direction which is intrinsically prohibited in the mechanical approach. As one example of the multi-directional alignment technique, the multi-rubbing process with the help of the screening by the sacrificial layer is shown in Fig. 2.12. A homogeneous alignment material AL22620 was spin-coated at the rate of 3000 rpm for 30 s on the glass substrate and annealed at 180°C for 1 h. The first rubbing, along the direction of R_1 as shown in Fig.2.12(a), was then carried out using the rubbing machine. The fluorinated polymer, EGC-1700 was transferred on to the alignment layer in the array of the square shape. The fundamental mechanism for the transfer printing was already described in Chapter 2.1. After that, the alignment layer was secondly rubbed along the direction of R_2 which was orthogonal to R_1 . Here, the transferred polymer patterns act as a role of the screening layer below which the rubbing direction is kept along the first rubbing direction. The lift-off

process was carried out by dipping the sample in the fluoruous-solvent HFE-7100. The chemical orthogonality prevailed between the alignment layer and the solvent while the screening layer was clearly washed out. As a result, the multi-domains with the directional preference in R_1 or R_2 were formed as shown in Fig. 2.12(c). The RM film was deposited on the predefined alignment layer by spin-coating of the mixtures of RM in solvent at the several conditions of the rate for 30 s. The RM film was softly annealed at 55°C for removing the solvent. Here, two mixtures of RM were used. The first mixture is RMS03-001C. The second mixture is the RM solution of a PGMEA containing four different acrylate-based mesogenic monomers: 4-(6-acryloyloxyhexyloxy)-benzoic acid (4-cyanophenyl ester), 4-(3-Acryloyloxypropyloxy)-benzoic acid 2-methyl-1,4-phenylene ester, 4-(6-Acryloyloxyhexyloxy)-benzoic acid-(4-methoxyphenylester), and 2-methyl-1,4-phenylene-bis[4-(6-acyloyloxyhexyloxy)benzoate] (RMS03-001C, Merck). The first mixture is capable of photo-polymerization under ambient condition while the second mixture requires nitrogen atmosphere for the polymerization. In other words, at the normal ambient condition or during the vacuum plasma treatment, the polymerization process for the second mixture is suppressed. It makes strong gradient of the polymerization and the distinct surface topography is formed in the micro-range period.

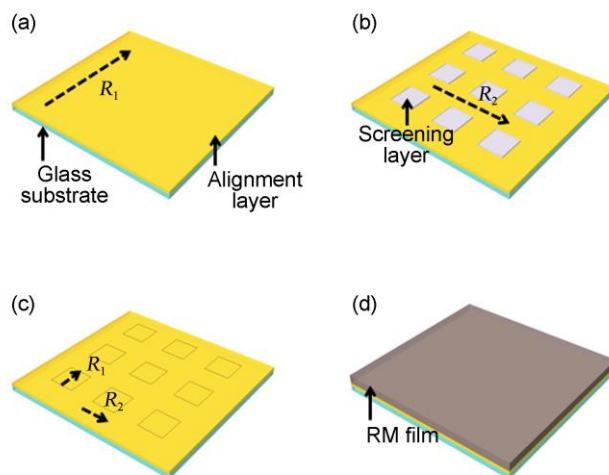


Figure 2.12. Schematic diagram showing the multi-directional rubbing process and the deposition of the RM film. (a) The alignment layer was firstly rubbed along the direction R_1 . (b) Transfer printing of the fluorinated polymer as a screening layer preserving the first rubbing during the second rubbing along R_2 . (c) Lift-off process of the screening layer. The multi-domains with the directional preference in R_1 or R_2 were formed. (d) The RM film was deposited by the spin-coating of the RM mixtures in solvent.

Results and discussion

Figure 2.13 shows the three different rubbing conditions of the alignment layer and the microscopic images of the RM film coated on the corresponding alignment layer. Here, RMS03-001 was used. On the un-rubbed surface as shown in Fig. 2.13(a), the wrinkles along the random direction were formed. It should be noted that the grains with the molecular orientation defined along one direction are

formed in micro-scale like the usual LCs, even though the RM was coated on the un-rubbed surface. It means that the characteristic length exists for determining the size of grain or the distance preserving the molecular orientation in one direction. If the period of the surface topography is relatively small with the characteristic length, the directional preference of topography was generated. On the rubbed alignment layer as shown in Fig. 2.13(b), the uniformly aligned wrinkles along the rubbing direction were formed. On the multi-directionally rubbed alignment layer, however, the direction of wrinkles is defined in a manner to release the elastic energy generated between two differently aligned domains. Thus, the wrinkles of which direction is continuously distributed occurred as shown in the microscopic images of Fig. 2.13(c).

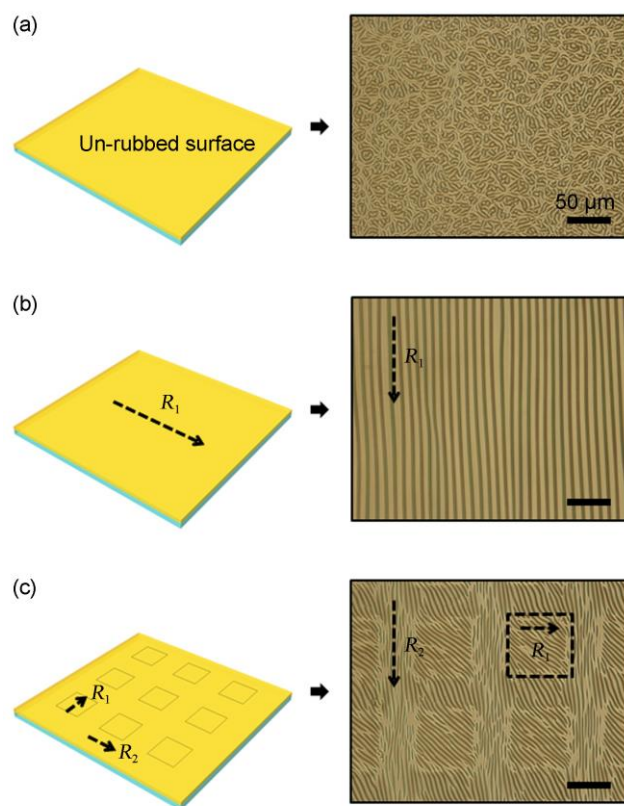


Figure 2.13. Three different rubbing conditions of the alignment layer and the microscopic images of the RM film coated on the corresponding alignment layer. (a) The un-rubbed alignment layer and the randomly formed wrinkles. (b) The rubbed alignment layer along the direction R_1 and the aligned wrinkles along the rubbing direction. (c) The multi-directionally rubbed alignment layer with the help of the screening layer and the wrinkles aligned in the two directions.

Figure 2.14 shows the surface topographies formed using two different RM

mixtures, RMS03-013C and RMS03-001. Both RM mixtures were coated on the rubbed alignment layer AL22620. The film of RMS03-013C was prepared by the spin-coating at the rate of 2000 rpm for 30 s. The surface topography was formed in two conditions of the plasma treatment: first sample was treated at the intensity of 150 W under 0.1 torr of oxygen for 30 s and the second sample was treated at the intensity of 150 W under 0.05 torr for 20 s. The AFM images of two samples are shown in Figs. 2.14(a) and 2.14(b), respectively. The film of RMS03-001C was prepared by the spin-coating at the two rates of 3500 rpm and 5500 rpm for 30 s. The plasma treatment was performed at the intensity of 150 W under 0.1 torr of oxygen for 30 s. The microscopic images of two samples are shown in Figs. 2.14(c) and 2.15(d), respectively. As described above, the two mixtures exhibit the different speed of the polymerization owing to the inherent material property. First mixture (RMS03-013C) is polymerized much faster than the second mixture (RMS03-001). This difference results in the surface topography in different scales ranging from tens of nanometer to a few micrometers. The relatively fast polymerization as in the case of RMS03-013C produces the nano-range surface topography where the directional preference of the topography was hardly observed. It means that the directional preference only appears at the period of topography over a critical point. Otherwise, the surface topography is formed in the isotropic bump shape as shown in Figs. 2.14(a), and 2.14(b). Since the period of the surface topography is primarily determined by the ratio between the polymerized hard layer and soft layer, it can be controlled by the modification of the plasma treatment and the thickness. The conditions for increasing period is the thicker film thickness, lower density or pressure of the plasma, and the longer exposure time of the plasma. At the smaller pressure condition (0.1 torr to 0.05

torr), the period of the topography was found to increase in spite of the reduced exposure time (30 s to 20 s), as shown in Fig. 2.14(b). It might be due to the fact that the pressure of plasma is related to the degree of the penetration. At the low penetration, only the surface of the RM film is polymerized so that the bi-layer configuration is clearly formed. Under the enough time of plasma treatment, the decrease of the film thickness directly contributes to the decrease of the un-polymerized soft layer. It resulted in the smaller period of the surface topography as shown in Fig. 2.14(d).

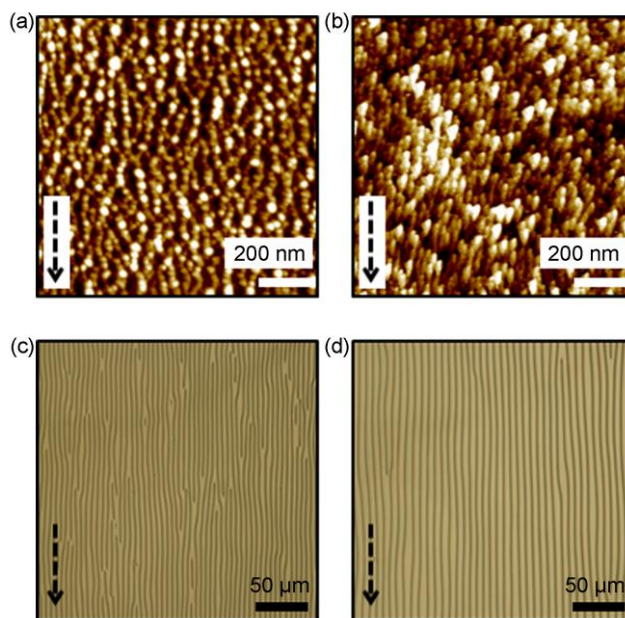


Figure 2.14. (a), (b) AFM images of the nanobumps on the RM film with the small depth-wise gradient of the polymerization. (c), (d) Microscopic images of the well-organized wrinkles along one direction on the RM film with the large depth-wise gradient of the

polymerization. Black dotted arrows represent the rubbing direction of the alignment layer.

2.5 Summary

In this chapter the aligning capability of the RM in the LC/RM composite system and the RM film in bi-layer configuration was discussed. At first, the patterns of polymerized RM in the LC/RM composite systems were constructed by the pattern formation of polymerized RM on the bottom substrate of LC cell. In both case of the horizontal and the vertical alignment of LC, the highly uniform alignment of LC across the RM patterns was achieved by the anisotropic directional preference of RM pattern. This uniform alignment was hindered in the LC/isotropic polymer composite system where the polymer patterns constructed through the transfer printing of fluorinated polymer, owing to the monotonic directional preference of the polymer. Second, the polymer-stabilization of LC induced by the photo-polymerization of RM initialized from the surface. In contrast with previous approaches, the photo-polymerization which is selectively initialized from surface forms the discrete parts of pure LC region and the LC/RM composite region in the separated configuration. Here, the chiral LC mixtures composed of RM, chiral dopant, and LC in various concentration ratios were prepared for studying the growth of polymer matrix and the optical spectrum depending on the density of RM. In the end of this chapter, the self-organization of surface structure induced by the buckling instability of the LCP layer is described. The

polymerization of RM film was carried out by the vacuum plasma treatment of which energy hardly penetrate the bulk of RM, so that the depth-wise gradual polymerization was achieved. During the plasma treatment, the RM film thermally swells. After cooling of RM film, the buckling instability between the polymerized region and soft region induces the nano-to-micro topography such as nanobumps and microwrinkles on surface. In addition, the initial alignment of RM on alignment layer induced the uniform wrinkles aligned along the direction of RM. The conditions of the polymerization are differed in a several way and the corresponding surface topography was experimentally observed.

Chapter 3

Tunable Color Elements Based on Chiral Reactive Mesogens

3.1 Introduction

Recently, the RLCDs have been attracted great attraction due to the outstanding outdoor performance with low power consumption [14-17]. The development of color reflectors with high quality is essential for constructing RLCDs since conventional color filters severely deteriorate the color gamut and reduce the total amount of the reflectance in the reflective mode. Moreover, the incident light passed the color filter twice and color filters can be differed in color depending on

the incident angle. As promising candidates, chiral nematic LCs (CLC) have been widely studied for such reflectors owing to the unique selective reflection characteristics arising from the periodic photonic band structure [18-21]. In addition, RMs are useful for stabilizing N* phase and providing the widened and/or shifted bandgap [22-26]. However, the full control of the reflectance in color by color without a band shift is still challenging for the case that only the modification or deformation of the helical pitch of the CLC is concerned.

In this chapter, a new type of RLCD based on the in-cell PSR of CRM will be demonstrated. Here, the PSRs were constructed through the spin-coating of a mixture of CRM, followed by the photo-polymerization process with the photomask. The PSRs exhibited the band reflection of the circular polarization component because it acts as a photonic bandgap structure. The reflectance was electrically tunable according to the phase retardation of the incident light through a homogeneously aligned LC layer, placed upon the PSR. The approach based on in-cell PSRs is directly applicable for constructing high-performance RLCDs.

3.2 Operation Principle

Figure 3.1 shows a schematic diagram illustrating the operation principle of RLCD based on the PSR. The proposed device is composed of the front polarizer, the LC layer, and the PSR. The phase retardation is denoted by Φ . It is well-known that the phase retardation of the LC layer can be varied by the voltage application due to the decrease of the Δn of LC. The incident light passed through the front

polarizer is linearly polarized at 45° with respect to the x axis. At the initial state as shown in Fig. 3.1(a), the LC layer with planar alignment where the slow axis of medium is parallel to x axis acts as a role of quarter-wave plate. The linearly polarized incident light then becomes the right-handed circular (RHC) polarized light after passing through the LC layer. The PSR placed after the LC layer reflects only the certain band of the wavelengths (green region in Fig. 3.1) and RHC polarization component of the incident light. The reflected light becomes vertically polarized light after passing through the LC layer and blocked by the front polarizer. At the state of the applied voltage as shown in Fig. 3.1(b), the polarization state of incident light becomes elliptical polarization after the LC layer and only RHC polarization component is reflected from PSR. The polarization state of reflected light becomes the elliptical polarization state again after the LC layer, and comes out from the device.

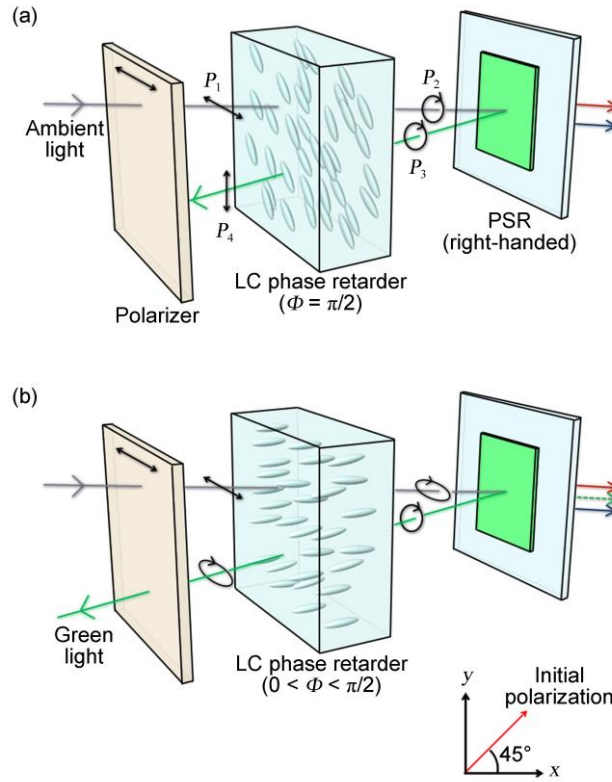


Figure 3.1. Schematic diagram illustrating the operation principle of RLCD based on the PSR of the CRM. (a) The initial dark state with the homogeneous alignment of LC where the reflected light blocked by the front polarizer. (b) The state of applied voltage with the reduction of phase retardation at the LC layer. The reflected light comes out from the device.

Stokes parameter

The Stokes parameters are a set of values which describe the polarization state

of light. The Stokes parameters are mathematically convenient alternative to the more common description of incoherent or partially polarized radiation in terms of its total intensity, degree of polarization, and the shape parameters of the polarization ellipse. The effect of an optical system on the polarization of light can be determined by constructing the Stokes vector for the input light and applying Mueller calculus, to obtain the Stokes vector of the light leaving the system. Here, brief information of Stokes vector and Mueller matrix will be given for calculating the optical response of our proposed system. The four quantities of stokes parameter of S_0 , S_1 , S_2 , and S_3 comprise the stokes vector which is described as

$$\vec{S} = \begin{bmatrix} S_0 \\ S_1 \\ S_2 \\ S_3 \end{bmatrix} \quad (3.1)$$

where S_0 denotes the time averaged total intensity of light. The parameters of S_1 , S_2 , and S_3 denote the relative intensity of the horizontal, $+45^\circ$, and RHC polarized light, respectively. When a parameter representing polarization component (S_1 , S_2 , and S_3) has a negative value, it has orthogonal polarization with respect to the positive value. For example, if S_1 is negative, it represents the vertical component of polarization. The four Stokes parameters are sometimes denoted by I , Q , U , and V , respectively. Compared to the Jones vector which handles only the space of fully polarized light, the Stokes vector spans unpolarized, partially polarized, and fully polarized light. In case of the unpolarized light, Stokes parameters are simply given as $I > 0$, and $Q = U = V = 0$. For the partially polarized light, the relationship between Stokes parameters is given as follow,

$$I^2 > Q^2 + U^2 + V^2. \quad (3.2)$$

For the fully polarized light, the relationship is given as

$$I^2 = Q^2 + U^2 + V^2. \quad (3.3)$$

The Stokes vectors for common states of polarization are shown in the Table 3.1.

Polarization state		Stokes vector
Linear polarization	Horizontal	$[1 \ 1 \ 0 \ 0]^T$
	Vertical	$[1 \ -1 \ 0 \ 0]^T$
	+45°	$[1 \ 0 \ 1 \ 0]^T$
	-45°	$[1 \ 0 \ -1 \ 0]^T$
Circular polarization	Right-handed	$[1 \ 0 \ 0 \ 1]^T$
	Left-handed	$[1 \ 0 \ 0 \ -1]^T$
Unpolarized irradiation		$[1 \ 0 \ 0 \ 0]^T$

Table 3.1. Stokes vectors for common states of polarization.

Mueller matrix

Mueller calculus is a matrix method for manipulating Stokes vectors. It was developed in 1943 by Hans Mueller. In this technique, the effect of a particular optical element is represented by a 4x4 matrix that is an overlapping generalization of the Jones matrix. The Mueller matrices for common optical elements are shown in the Table 3.2.

Optical elements		Mueller matrix
Linear polarizer	Horizontal transmission	$\frac{1}{2} \begin{bmatrix} 1 & 1 & 0 & 0 \\ 1 & 1 & 0 & 0 \\ 0 & 0 & 0 & 0 \\ 0 & 0 & 0 & 0 \end{bmatrix}$
	Vertical transmission	$\frac{1}{2} \begin{bmatrix} 1 & -1 & 0 & 0 \\ -1 & 1 & 0 & 0 \\ 0 & 0 & 0 & 0 \\ 0 & 0 & 0 & 0 \end{bmatrix}$
	+45° transmission	$\frac{1}{2} \begin{bmatrix} 1 & 0 & 1 & 0 \\ 0 & 0 & 0 & 0 \\ 1 & 0 & 1 & 0 \\ 0 & 0 & 0 & 0 \end{bmatrix}$
	-45° transmission	$\frac{1}{2} \begin{bmatrix} 1 & 0 & -1 & 0 \\ 0 & 0 & 0 & 0 \\ -1 & 0 & 1 & 0 \\ 0 & 0 & 0 & 0 \end{bmatrix}$
Wave plate	Quarter wave plate (vertical fast-axis)	$\begin{bmatrix} 1 & 0 & 0 & 0 \\ 0 & 1 & 0 & 0 \\ 0 & 0 & 0 & -1 \\ 0 & 0 & 1 & 0 \end{bmatrix}$

Quarter wave plate (horizontal fast-axis)	$\begin{bmatrix} 1 & 0 & 0 & 0 \\ 0 & 1 & 0 & 0 \\ 0 & 0 & 0 & 1 \\ 0 & 0 & -1 & 0 \end{bmatrix}$
Half wave plate	$\begin{bmatrix} 1 & 0 & 0 & 0 \\ 0 & 1 & 0 & 0 \\ 0 & 0 & 1 & 0 \\ 0 & 0 & 0 & 1 \end{bmatrix}$

Table 3.2. Mueller matrices for common optical elements.

Mueller calculus for reflectance

The reflectance of proposed configuration as a function of the phase retardation can be predicted by using Stokes vector and Mueller calculus. Considering the incident light as the unpolarized light with the intensity of I_{in} , the stokes vector for the polarization state right after the front polarizer (P_1) is described as

$$P_1 = M_1 P_0 = \frac{1}{2} \begin{bmatrix} 1 & 0 & 1 & 0 \\ 0 & 0 & 0 & 0 \\ 1 & 0 & 1 & 0 \\ 0 & 0 & 0 & 0 \end{bmatrix} \begin{bmatrix} I_{\text{in}} \\ 0 \\ 0 \\ 0 \end{bmatrix} = \frac{I_{\text{in}}}{2} \begin{bmatrix} 1 \\ 0 \\ 1 \\ 0 \end{bmatrix}, \quad (3.4)$$

where P_0 and M_1 denote the Stokes vector of the incident light and the Mueller matrix for the front polarizer, respectively. The LC layer is tunable phase retarder of which slow axis is parallel to the x axis. The Mueller matrix for LC layer (M_2) can be described using the phase retardation, Φ .

$$M_2 = \begin{bmatrix} 1 & 0 & 0 & 0 \\ 0 & 1 & 0 & 0 \\ 0 & 0 & \cos\Phi & -\sin\Phi \\ 0 & 0 & \sin\Phi & \cos\Phi \end{bmatrix}. \quad (3.5)$$

The stokes vector for the light passed through the LC layer (P_2) is then described as

$$P_2 = M_2 P_1 = \frac{I_{\text{in}}}{2} \begin{bmatrix} 1 \\ 0 \\ \cos\Phi \\ \sin\Phi \end{bmatrix}. \quad (3.6)$$

P_2 corresponds to the elliptical polarization state which is equal to the sum of linear polarization and circular polarization state. Since the PSR reflects only the RHC polarized light, the Stokes vector of the reflected light has only RHC polarization component.

$$P_3 = \frac{I_{\text{in}}}{2} \left(\sin\Phi + \frac{1}{2} \cos\Phi \right) \begin{bmatrix} 1 \\ 0 \\ 0 \\ 1 \end{bmatrix}. \quad (3.7)$$

In the inverse direction of light propagation mode, the slow axis of LC layer is still parallel to the x axis so that the Mueller matrix for LC layer is equal to M_2 . The transmission angle of the front polarizer, however, changes from $+45^\circ$ to -45° . Mueller matrix for front polarizer for the inverse propagation mode (M_3) is described as,

$$M_3 = \frac{1}{2} \begin{bmatrix} 1 & 0 & -1 & 0 \\ 0 & 0 & 0 & 0 \\ -1 & 0 & 1 & 0 \\ 0 & 0 & 0 & 0 \end{bmatrix}. \quad (3.8)$$

Finally, the Stokes vector of output light (P_4) is obtained as follow,

$$P_4 = M_3 M_2 P_3 = \frac{I_{\text{in}}}{4} \cos \Phi \left(\sin \Phi + \frac{1}{2} \cos \Phi \right) \begin{bmatrix} 1 \\ 0 \\ -1 \\ 0 \end{bmatrix}. \quad (3.9)$$

Thus, the intensity of the output light (I_{out}) by that of the input light as a function of Φ is driven as,

$$\frac{I_{\text{out}}}{I_{\text{in}}} = \frac{\cos \Phi}{4} \left(\sin \Phi + \frac{1}{2} \cos \Phi \right), \quad (3.10)$$

where Φ is in range from $\pi/2$ to 0.

Description on Poincaré sphere

Figure 3.2 describes the optical pathway of the polarization on the Poincaré sphere. The incident light with linear polarization of 45° with respect to x axis corresponds to the point of $+S_2$. The light passed through LC layer rotates from $+S_2$ in a counter clockwise (CCW) direction in the S_2 - S_3 plane by the amount of Φ . In case of $\Phi = \pi/2$ as can be seen in Fig. 3.2(a), the light becomes RHC polarized state and is totally reflected in front of the PSR. The polarization state of reflected light is $-S_3$ and experiences the same optical pathway of the incident light so that the

polarization state of the light after the LC layer becomes S_2 by the $\pi/2$ of CCW rotation from $-S_3$ which is equal to the orthogonal direction to the transmission axis of the front polarizer for the inverse propagation mode. In the case of $0 < \Phi < \pi/2$ as shown in Fig. 3.2(b), the polarization state of the light in front of the PSR is located between $+S_2$ and $+S_3$. Thus, only the RHC polarization component which is scaled by $\sin\Phi + \cos\Phi/2$ is reflected. During the inverse propagation mode, the reflected light becomes the elliptical polarization state again (between $-S_3$ and $+S_2$). This polarization state can be considered as the sum of linear polarization at $+45^\circ$ and the LHC polarization. Finally, the -45° linear polarization component of reflected light comes out from device.

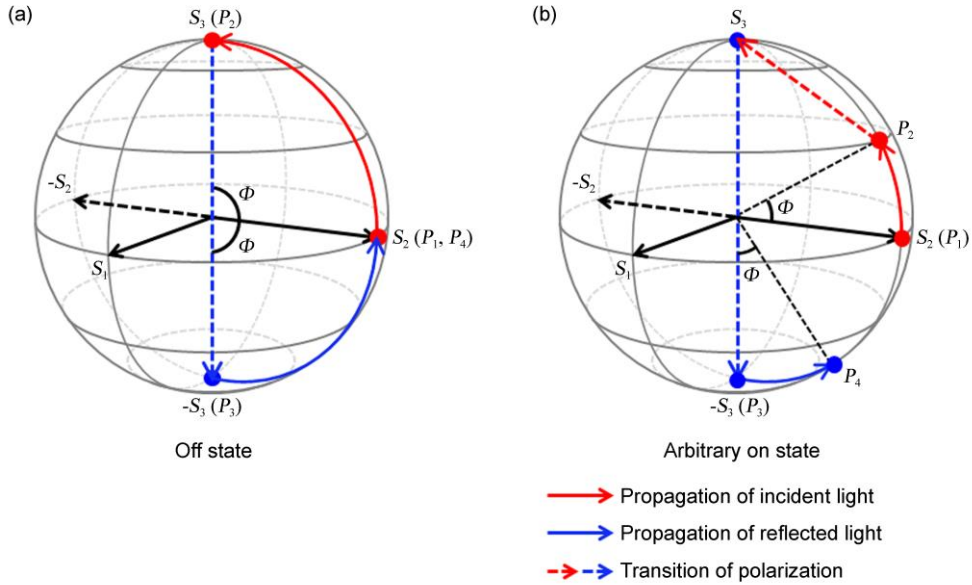


Figure 3.2. Schematic diagram of optical pathways for (a) the initial off state and (b) the state of arbitrary on state by the applied voltage. Here, the red arrows and the blue arrows represent the propagation of

incident light and reflected light, respectively and the dashed arrows represent the transition of polarization.

3.3 Fabrication Process

The material used in this study was a solution of acrylate-based chiral LC monomers with reactive mesogenic groups, RMS11-066, 067, and 068 (Merck). These are composed of various reactive acryloyloxy mesogens in toluene with the different ratio for exhibiting different selective reflection wavelength. The peak wavelength of RMS11-066, 067, and 068 is about 424 nm, 530 nm, and 631 nm, respectively. In the experiment, three mixtures for red (R), green (G), and blue (B) (M_R , M_G , and M_B) is prepared by blending RMS11-066, 067, and 068. M_R is a mixture of RMS11-067 and 068 at 1:9 blending in the weight ratio. M_G is a mixture of RMS11-067 and 068 at 9:1 blending in the weight ratio. M_B is a mixture of RMS11-066 and 067 at 7:3 blending in the weight ratio. The peak wavelength of M_R , M_G , and M_B is about 460 nm, 540 nm, and 620 nm, respectively.

A homogeneous alignment layer (AL22620) was prepared on the inner surface of the indium-tin-oxide (ITO)-coated substrate by spin coating at the rate of 3000 rpm for 30 s and post-annealed at 180°C for 1 h. The rubbing directions on the top and bottom substrates were parallel to each other. For the construction of PSR for R (PSR-R), the M_R was spin-coated at the rate of 2000 rpm for 30 s on the bottom substrate and dried at 55°C for 60 s to remove the residual solvent. The layer of M_R was photo-polymerized with the photomask by the exposure of UV at the intensity

of 20 mW/cm² for 120 s. The un-polymerized materials were washed out by the toluene (Sigma Aldrich Korea) and dried at 75 °C. The PSR for G (PSR-G) and PSR for B (PSR-B) were constructed using M_G, and M_B by same process as described above. The cell gap (d) is maintained to be 3.5 μm using glass spacers and the positive LC, ZLI-1800-1005 ($n_e = 1.5503$, $\Delta n = +0.0705$, Merck) was infiltrated by the capillary action. Note that the thickness of each PSR layer is varied according to the peak wavelength for satisfying the quarter-wave retardation of LC layer. The relationship between the phase retardation of LC layer and thickness of PSR (h_k) can be described as

$$\Phi = \frac{2\pi}{\lambda_k} \Delta n (d - h_k), \quad (3.11)$$

where λ_k denotes the peak wavelength of the PSR and the numbering k is applied to R, G, and B in sequence. From the condition of the 3.5 μm cell gap, the thickness of PSR-R, PSR-G, and PSR-B for the quarter-wave retardation is driven as 1.3 μm, 1.6 μm, and 1.9 μm.

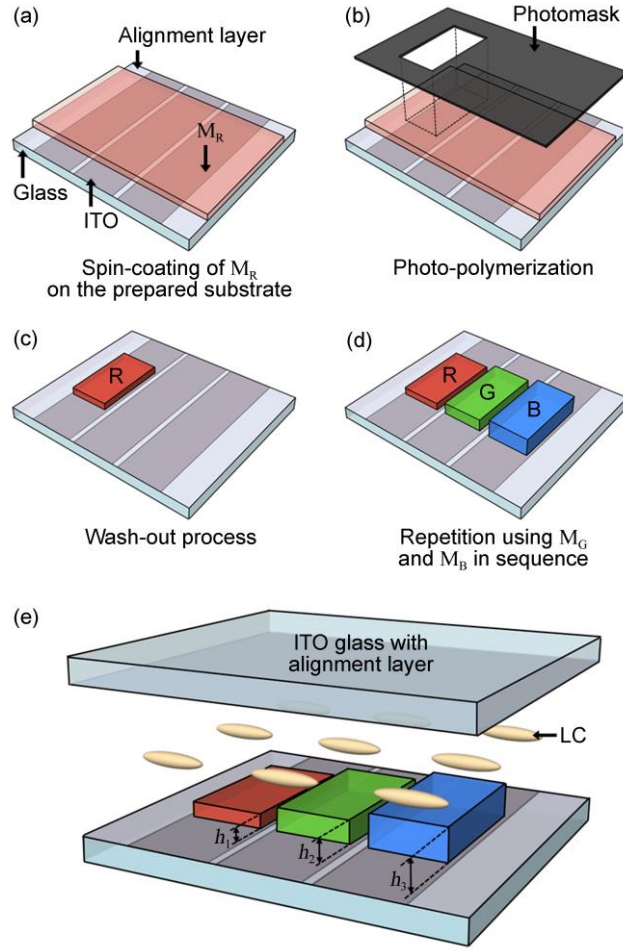


Figure 3.3. Fabrication process of the RLCD based on the PSR of the CRM. (a) Spin-coating of M_R on the prepared bottom ITO substrate. (b) Photo-polymerization of the M_R layer using the photomask. (c) Wash-out process for the removal of the residual material. (d) Repetition using M_G and M_B in sequence. (e) Construction of the cell and the infiltration of LC.

3.4 Results and Discussion

Figure 3.4 shows the microscopic images of the reflection of each color element by a PSR array in a rectangular shape as a function of the applied voltage. The three types of the PSR were arranged in the independent cell. The width (W_a) and the length of each PSR were about 100 μm and 300 μm , respectively. The gap or separation (W_b) between adjacent PSR was about 200 μm . The transmission axis of the front polarizer and the rubbing direction were denoted by P and R , respectively. In all the case, the reflectance was found to monotonically increase as the applied voltage increases. The increase of applied voltage enables to reduce the phase retardation of the LC layer in the proposed configuration so that the reflectance increases. It agrees well with the calculation performed above. Note that the light leakages shown in the several images are owing to the alignment distortion of PSR layer which is primarily resulted from the point defects of the alignment layer.

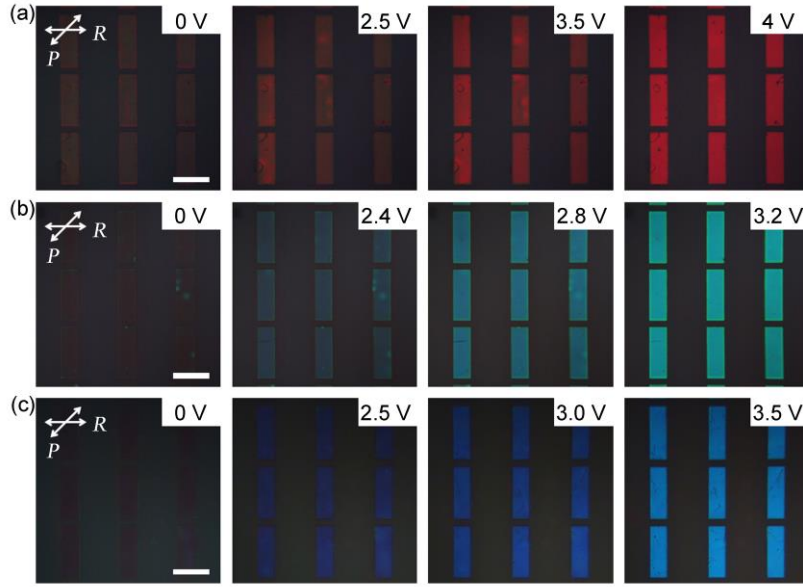


Figure 3.4. Microscopic images of the reflection of (a) R, (b) G, and (c) B by the PSR array in a rectangular shape depending on the applied voltage.

Voltage-dependent reflectance

The voltage-dependent reflectance from three R, G, and B elements was measured. The coherent light source with the peak wavelength of 633 nm, 544 nm, and 465 nm was used for the measuring of the reflectance of R, G, and B, respectively. In the optical setup, the transmission axis of the polarizer placed in front of the cell and the rubbing direction of the cell is equal to that shown in Fig. 3.4. As can be seen Fig. 3.5, as the applied voltage increases, the normalized reflectance increases from 0 to 1. It is due to the decrease of Φ from $\pi/2$ to 0. Here, the value of threshold voltage was defined as the voltage where the difference of the reflectance was 2% of the reflectance at no applied voltage. The threshold

voltage was measured to be around 2.1 V.

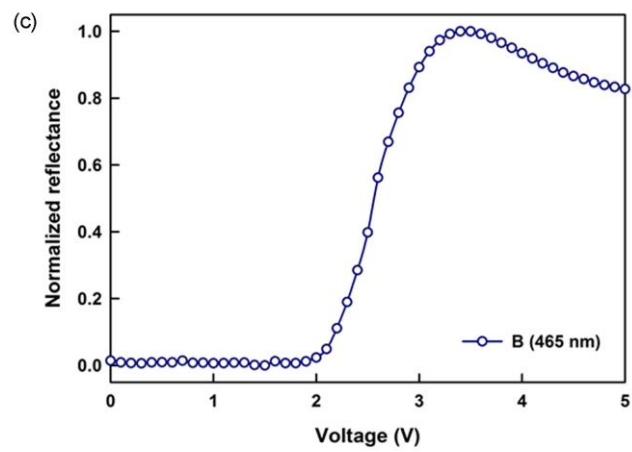
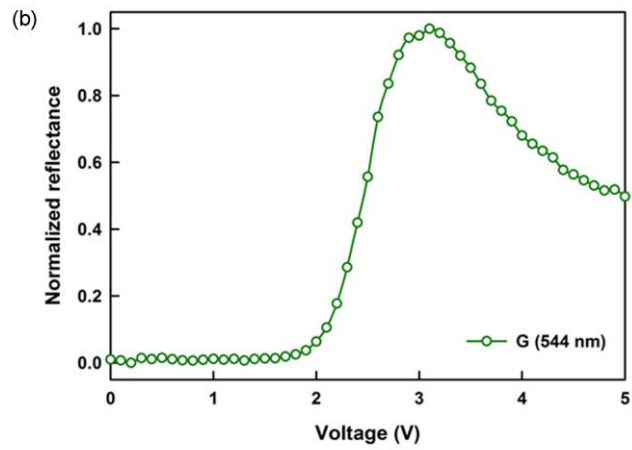
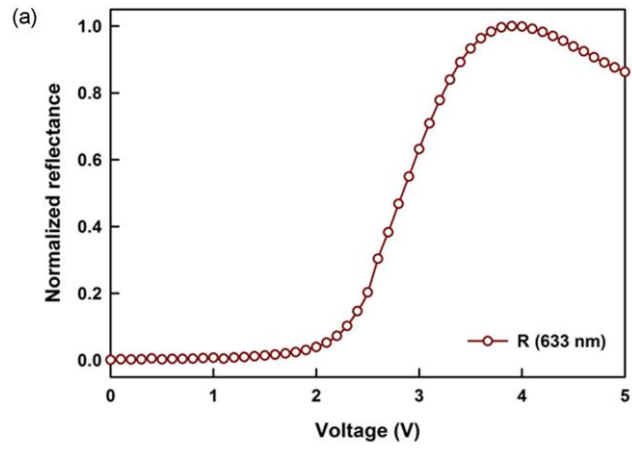


Figure 3.5. The normalized voltage-dependent reflectance of the (a) R, (b) G, and (c) B elements.

Dynamic response

The dynamic response of the cell (PSR-R) was measured in order to estimate the electro-optical response time. The digitizing oscilloscope (Waverunner 6040, Lecroy) and the He-Ne laser with the peak wavelength of 633 nm were used for the measurement. The electric source with bipolar square waveform with frequency of 1 kHz and amplitude of 4 V was applied by a function generator (DS 345, Stanford Research Systems). The response time was measured as 46 ms for rising and 64 ms for fall, as shown in Fig.3.6.

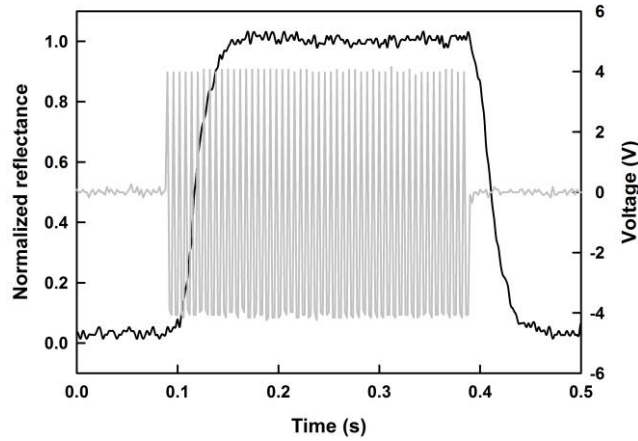


Figure 3.6. Dynamic response of the cell based on the PSR-R.

Optical spectrum

Figure 3.7 shows reflection spectra of each color. For measuring the reflectance, a deuterium halogen light source and a UV-Vis. fiber optic spectrometer (Ocean Optics S2000) were used. Here, the homogeneous LC cell without the PSR was used as reference. As shown in Fig. 3.7 the bandwidth of each color was measured as 460 ± 42 nm, 540 ± 43 nm, and 620 ± 42 nm, respectively. As the applied voltage increases, the reflectance increases while the value of peak wavelength and the bandwidth were maintained. Such tunable reflectance preserving the bandwidth is mainly resulted from the separation between the element for the color generation (reflection by PSR) and that for the intensity control (phase retardation by LC). At the best of our knowledge, this approach has not been made so far from previous research related to the tunable reflection by CLC.

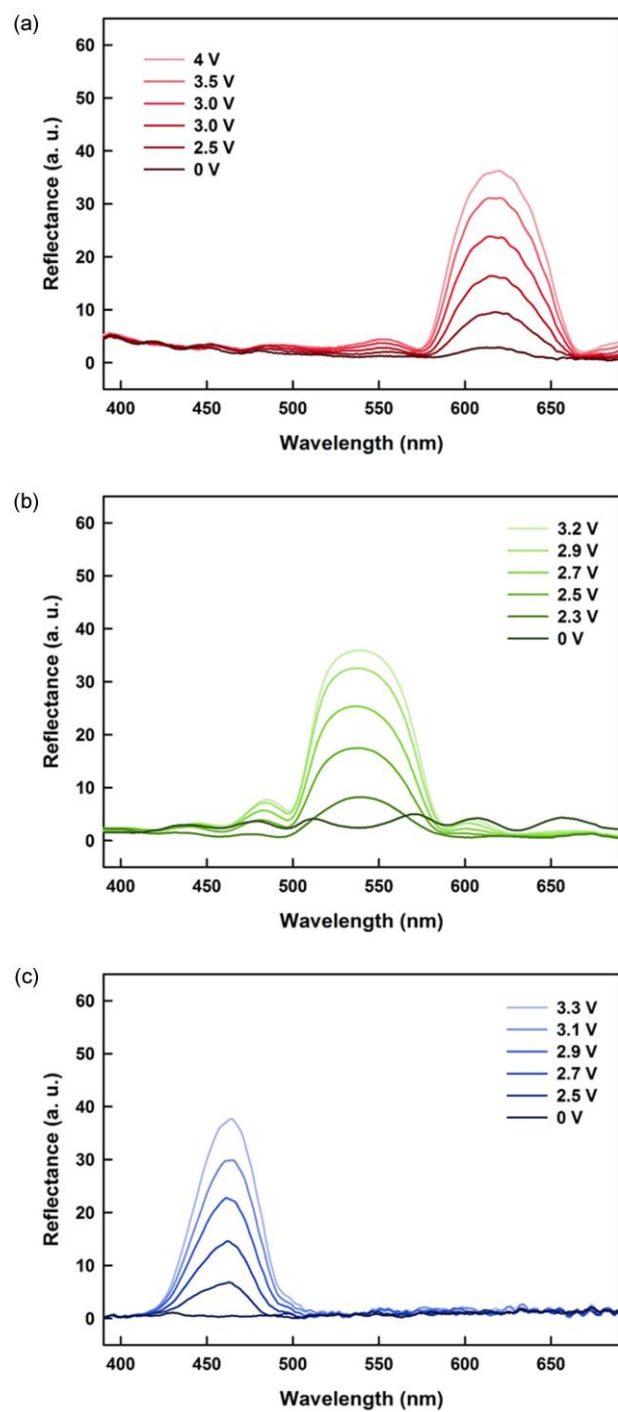


Figure 3.7. Optical spectrum of the (a) R, (b) G, and (c) B depending

on the applied voltage.

Demonstration of prototype

Finally, a simple prototype of RLCD, incorporated with the three PSR for the primary colors of R, G, and B was fabricated for the purpose of proving the above concept. Here, the patterned ITO on a glass substrate was used as the bottom electrode. Each PSR was patterned for representing the three letters of “S”, “N”, and “U” and vertically arranged on the bottom substrate. Note that the scalability to smaller dimensions primarily depends on the size (or resolution) of the photomask. Figure 3.8 show the microscopic image of our LC cell. While the normally reflectance state for three colors was obtained under no applied voltage as shown in Fig. 3.8(a), the diminishing reflectance of the different colors of R, G, and B from pixel to pixel were clearly observed under the applied voltage of 5 V as shown in Figs. 3.8(b), (c), and (d). The unit pixels of R, G, and B colors can be independently operated by the application of different voltages to the patterned ITO electrodes. Note that PSR indeed provides the tunable color reflection capability for the RLCD as an alternative to a conventional color filter.

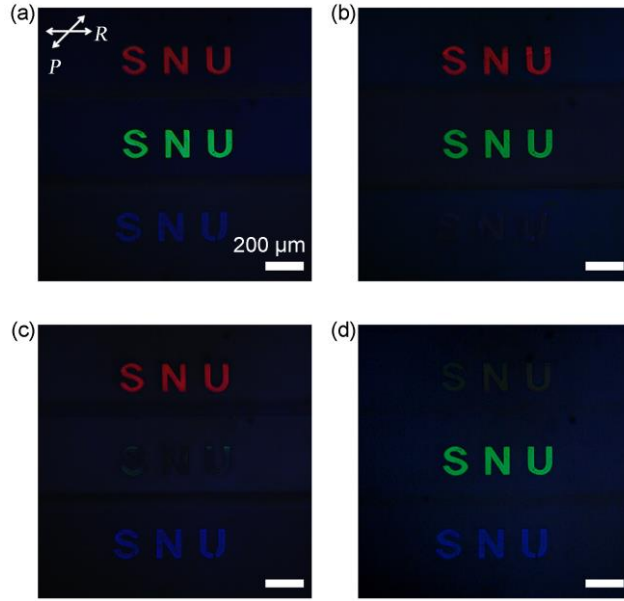


Figure 3.8. Microscopic images for the prototype demonstration of the proposed RLCD incorporated with the three PSR for the primary colors of R, G, and B.

3.5 Summary

In this chapter, a new concept of RLCD based on the PSR was proposed. In contrast to the conventional color filter, the PSR is capable of selecting the color and serves as a tunable reflector depending on the wavelength of the incident light. The remarkable high reflectance and color uniformity is mainly due to the separation of the element for the color generation and that for the intensity control,

which has not been made so far. The prototype of RLCD exhibiting the reflection of three basis colors, R, G, and B was demonstrated. The PSR-based approach will provide a new method of achieving the high image quality of the RLCD.

Chapter 4

Reduction of Color Shift by Reactive Mesogen Layer

4.1 Introduction

The invariance of the color uniformity at oblique viewing angles has been one of the critical challenges in LCDs where the gamma distortions in the off-axis results primarily from the difference in the effective optical pathway among different viewing directions. A simple way of reducing the gamma distortions is the use of an extra birefringence film to compensate for the phase retardation change depending on the viewing direction [27, 28]. Another one relies on the pixel-division into sub-domains with different directions of the LC alignment through either the use of patterned electrodes or the modification of the alignment layer

[29-33]. In the pixel-division approach, the gamma distortions can be further reduced using multiple driving transistors [34-37], the variations of the anchoring energy [38, 39], structured electrodes [40-42], or voltage dividing layers (VDLs) [43, 44]. Among them, the use of the VDL provides a reliable and effective way of reducing the gamma distortions by means of the shift of the threshold voltage. However, existing VDL methods involve a series of complicated processes, particularly, for the uniform alignment of LCs on the VDL. Note that the isotropic nature of the conventional VDL causes the variations of the pretilt angle at the boundaries between the sub-domains.

In this chapter, a new approach to the reduction of the gamma distortions by the introduction of an AVDL constructed using RMs will be demonstrated. The underlying concept is based on the voltage division by the AVDL which is capable of shifting the threshold voltage in sub-domain by sub-domain as well as spontaneously aligning the LC without any additional surface treatment. The AVDL was constructed through the blanket deposition of the RM by simple spin-coating and the subsequent selective photo-polymerization of the RM under the UV exposure with a predefined photomask, followed by the removal of the remnant RM. It was found that the UV exposure time for the photo-polymerization of the RMs plays a crucial role in the stable and uniform alignment of the LC on the AVDL. For the assessment of the off-axis image quality, numerical simulations together with the experimental measurements were performed to obtain the gamma curves in the vertical alignment configuration with 4-domain electrodes.

4.2 Operation Principle

The conceptual diagrams showing the conventional isotropic VDL (IVDL) and AVDL in the vertical alignment mode are depicted in Fig. 4.1. In case of the IVDL as shown in Fig. 4.1(a), the LC alignment near the IVDL boundaries is substantially disturbed and thus, the light leakage near the boundaries is inevitably involved as clearly seen in the microscopic image observed under crossed polarizers. In the AVDL case as shown in Fig. 4.1(b), however, the uniform LC alignment is obtained across the AVDL owing to the self-aligning capability of the RMs. In other words, the AVDL requires no planarization process for the uniform LC alignment and allows the simplicity in fabrication. In the presence of an applied voltage, the AVDL acted as a capacitive element to yield the difference of the threshold voltage in sub-domain by sub-domain. This threshold difference enabled to compensate for the difference of the phase retardation between the normal viewing direction and an oblique viewing direction so that the off-axis gamma distortions could be reduced in a simple way.

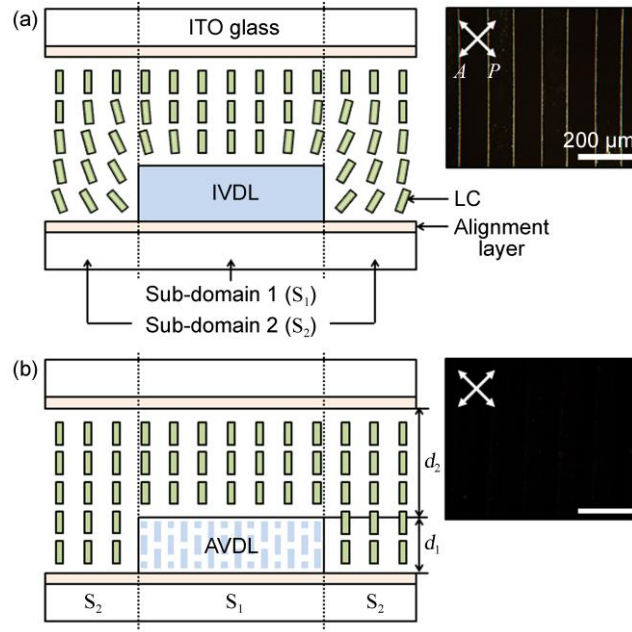


Figure 4.1. The conceptual diagrams of the LC cell with (a) the IVDL and (b) the AVDL in the vertical alignment mode. Here, d_1 , d_2 denote the thickness of the AVDL and that of the LC layer in the bulk, respectively. The microscopic textures were taken under crossed polarizers (A: analyzer and P: polarizer).

4.3 Numerical Calculation

It was carried out that two-dimensional simulations of the luminance at the input grey scales of 256 and the gamma curves for different values of the AVDL thickness (d_1) in a PVA configuration. Basically, the profiles of the LC director were calculated as a function of an applied voltage from an iterative solution for

the minimization of the free energy in the finite element method [45]. The voltage-dependent transmittance was accordingly obtained from the LC director profiles. The theoretical description for calculating the distribution of LC directors is briefly given below.

4.3.1 Theoretical description

Elastic free energy density

In the N phase satisfying the cylindrical symmetry and the absence of the polarity, the Frank-Oseen elastic free energy in terms of the splay, twist, bend deformation is described as

$$f_{\text{elas}} = \frac{1}{2} K_1 (\nabla \cdot \mathbf{n})^2 + \frac{1}{2} K_2 (\mathbf{n} \cdot \nabla \times \mathbf{n})^2 + \frac{1}{2} K_3 (\mathbf{n} \times \nabla \times \mathbf{n})^2, \quad (4.1)$$

where K_1 , K_2 , and K_3 denote the elastic coefficients of the splay, the twist, and the bend deformations, respectively.

Electrostatic energy density

When an electric field is applied to LC, the coupling of the electric field (\mathbf{E}) and the electric displacement (\mathbf{D}) generates a rotational torque. The electric displacement is described as

$$\mathbf{D} = \varepsilon_{\perp} \mathbf{E} + (\varepsilon_{\parallel} - \varepsilon_{\perp}) (\mathbf{n} \cdot \mathbf{E}) \mathbf{n}, \quad (4.2)$$

where ε_{\parallel} and ε_{\perp} denote the static dielectric constant along and normal to the LC

director (\mathbf{n}), respectively. The electrostatic energy density is then obtained as

$$f_{\text{elec}} = -\frac{1}{2} \mathbf{D} \cdot \mathbf{E} = -\frac{1}{2} \Delta\epsilon (\mathbf{n} \cdot \mathbf{E})^2 - \frac{1}{2} \epsilon_{\perp} \mathbf{E}^2, \quad (4.3)$$

where $\Delta\epsilon = \epsilon_{\parallel} - \epsilon_{\perp}$. Here, the reorientation of the LC is determined depending on the sign of $\Delta\epsilon$. For $\Delta\epsilon > 0$, the LC is reoriented along the direction of the electric field while for $\Delta\epsilon < 0$, LC is reoriented in the perpendicular direction of the electric field.

Surface anchoring energy density

In general case, the surface anchoring energy density is taken into account at the boundaries of the system. It means that the director values of the LC at the boundaries changes by the electrical field. From the Rapini-Papoular model, the surface anchoring energy density can be driven as

$$f_{\text{surf}} = \frac{1}{2} A_p \sin^2(\theta - \theta_0) + \frac{1}{2} A_a \sin^2(\varphi - \varphi_0), \quad (4.4)$$

where A_p and A_a denote the polar anchoring strength and the azimuthal anchoring strength, respectively, and θ and φ denote the polar angle and the azimuthal angle of tilted LC from the initial polar angle (θ_0) and azimuthal angle (φ_0), respectively. Under an assumption of strong anchorage or infinite anchorage, the director values are fixed regardless of the electric field.

Total free energy

The total free energy is equal to the summation of the bulk energy and the surface anchoring energy as described in follow,

$$F_{\text{tot}} = F_{\text{bulk}} + F_{\text{surf}} = \iiint f_{\text{elec}} + f_{\text{elas}} dx dy dz + \iint f_{\text{surf}} dx dy. \quad (4.5)$$

The distribution of LC director in equilibrium state can be obtained by minimizing the total free energy.

Simulation parameters

The voltage-dependent transmittance for calculating the gamma curves was solved using the LC director profile. The top and bottom alignment surface including the surface of the AVDL were considered as the strong anchoring region and initial condition of the polar angle of LC director was 90° . Note that the initial alignment state of the LC near the AVDL was perpendicular to the substrate, not to the lateral side of the AVDL. The cell gap was $5 \mu\text{m}$ and the parameters of the LC used in this calculation were matched with the negative LC, MLC-2037 (Merck). The material parameters are the parallel and perpendicular components of the dielectric constant of the LC $\varepsilon_{\parallel} = 3.6$ and $\varepsilon_{\perp} = 6.7$, the ordinary refractive index $n_o = 1.4722$, the extraordinary refractive index $n_e = 1.5371$, the splay elastic constant $K_{33} = 18.1 \text{ pN}$, and the viscosity $\gamma_1 = 132 \text{ mPa}\cdot\text{s}$. The dielectric constant of the AVDL was determined to be 2.55 from the measured capacitance. The monochromatic light (550 nm) with the angular power distribution following Lambert's law was used as an incident light source.

4.3.2 Simulation result of gamma distortion

Figures 4.2(a) and 4.2(b) show the top views of two unit cells without the AVDL (4 domains) and with the AVDL (8 domains), respectively, in the PVA

configuration with simple chevron electrodes [46, 47]. Two-dimensional simulations for the voltage-dependent transmittance were carried out in a symmetric unit cell with the azimuthal angle $\varphi = 0^\circ$ as shown in Fig. 4.2(c). This cell corresponds to the cross-section along the red line in Fig. 4.2(b) which is translated by one quarter of the lateral dimension of the original unit cell shown in the bottom of Fig. 4.2(b). The gamma curves, representing the output luminance as a function of the intended input grey levels, were obtained from the voltage-dependent transmittance at different polar angles. The number of the input grey levels was 256 in the range of the applied voltage from 2.2 V to 5 V. The luminance was simply the transmittance.

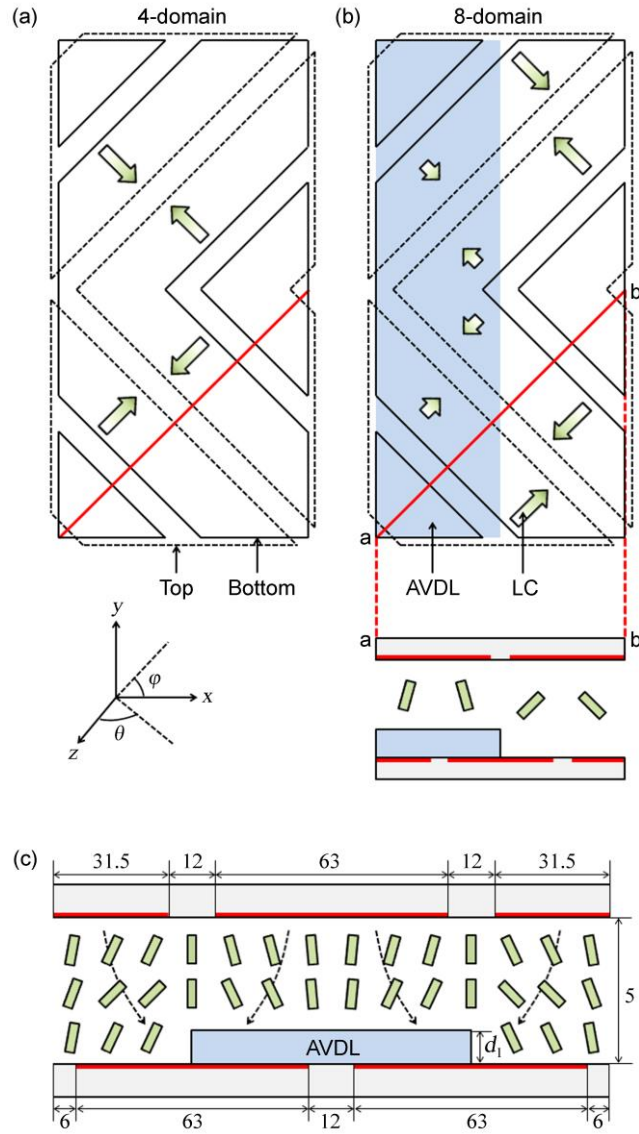


Figure 4.2. The schematic illustration of the top views of the LC unit cells (a) without the AVDL (4-domain) and (b) with the AVDL (8-domain). Black lines and dotted lines represent the bottom and top electrodes, respectively. The direction and the amount of tilt angle of the LC in the sub-domains are represented by the arrows. Red lines

represent the cross-section lines for two-dimensional simulations. The cross sectional view of a unit cell with the AVDL is shown in the bottom of (b). (c) A symmetric unit cell corresponding to the cross-section along the red line for two-dimensional simulations. Black dotted lines in the cell represent the electrical field lines. Here, the geometrical parameters are given in the unit of μm .

The amount of the gamma distortions along an arbitrary off-axis can be represented by the gamma distortion index (GDI), D , which is given as [34]

$$D(\theta, \varphi) = \frac{1}{n^2} \sum_i \sum_j \left| \frac{\Delta B_{ij} - \Delta B'_{ij}(\theta, \varphi)}{\Delta B_{ij}} \right|, \quad (4.6)$$

where ΔB_{ij} and $\Delta B'_{ij}$ denote the difference of the luminance between i th and j th grey level at on-axis and at off-axis of polar angle (θ) , and azimuthal angle (φ) , respectively. The total number of the grey levels is n . For a smaller value of D , a smaller amount of the gamma distortions is expected. Figures 4.3(a) and 4.3(b) show the simulation results for the gamma curves for $d_1 = 0 \mu\text{m}$, and $d_1 = 0.6 \mu\text{m}$, respectively. It is clearly seen from Fig. 4.3(b) that in the presence of the AVDL, the GDI was greatly reduced particularly in the low range of the grey levels. Another point is that from the plot of D as a function of d_1 shown in Fig. 4.3(c), the reduction of the GDI was effectively achieved in a certain range of d_1 (from about 0.5 to $0.9 \mu\text{m}$) at all viewing angles, meaning that a proper thickness of the AVDL should be chosen. Moreover, since the GDI depends on not only the angular distribution of the phase retardation but also the ratio of the transmittance between

the sub-domains, the relative area of the AVDL in the unit cell should be taken into account.

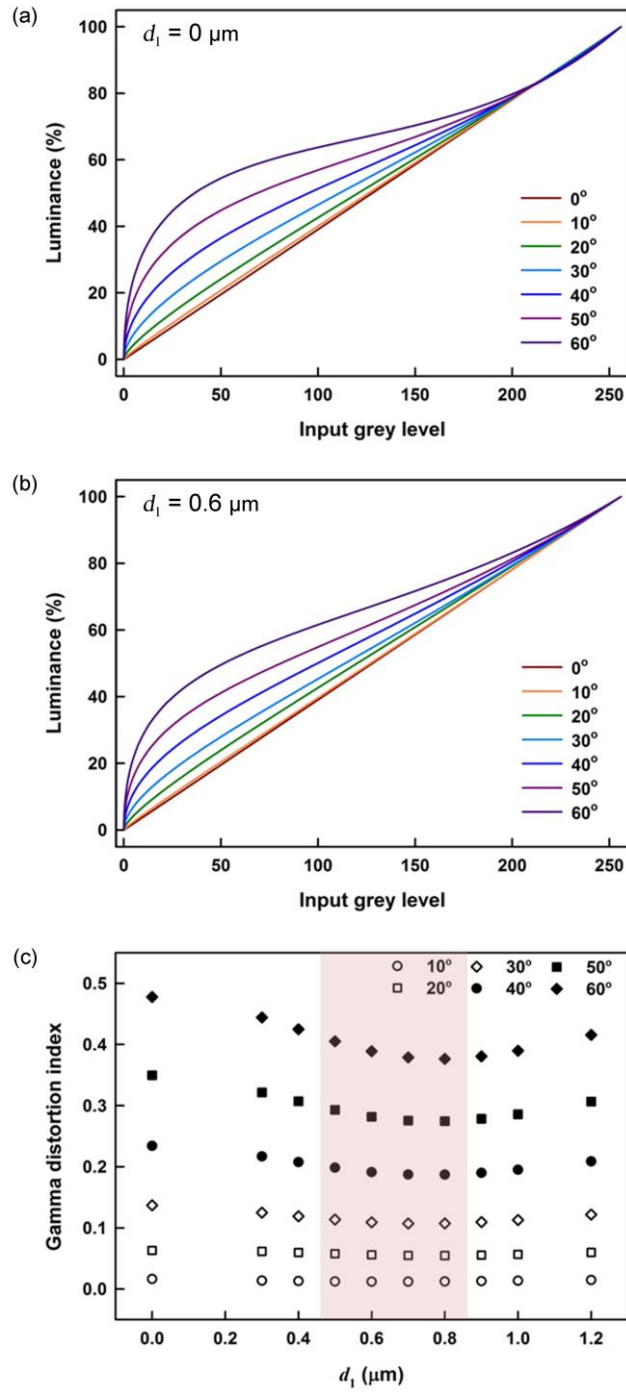


Figure 4.3. Simulation results for the luminance as a function of the

input grey level (gamma curves) for different values of the polar angles ($\theta = 0^\circ$ to 60° at $\varphi = 0^\circ$) for (a) $d_1 = 0$ and (b) $d_1 = 0.6 \mu\text{m}$. (c) The calculated GDI as a function of the AVDL thickness for different polar angles from 0° to 60° . The range of the proper thickness of the AVDL for the effective reduction of the GDI value is represented by the region in red.

4.4 Experiment

4.4.1 Fabrication process

Using the electrode used for the numerical calculation, the LC cell with the patterned AVDL ($d_1 = 0.57 \mu\text{m}$) was fabricated as shown in Fig. 4.4. In fabricating the LC cells, ITO-coated glass substrates were spin-coated with a homeotropic alignment material (AL60702) at the rate of 3000 rpm for 30 s and post-annealed at 150°C for 1 h. A mixture of the RMs with photo-initiator (RMS03-015) was then spin-coated at the rate of 3000 rpms for 30 s on the alignment layer. The RM layer was kept under ambient condition for 60 s to remove the residual solvent and subsequently exposed to UV at the intensity of $20 \text{ mW}/\text{cm}^2$ for several different times of 30 s, 60 s, 90 s, and 120 s through a predefined photomask for photo-polymerization. After washing out the un-polymerized RMs with p-xylene (Sigma Aldrich Korea), the substrate was dried at 60°C for 1h. The surface morphology of the AVDL was observed using an atomic force microscope (AFM) (XE-150; PSIA)

in the non-contact mode and the corresponding surface energy was measured using the harmonic mean method [48] from the contact angles of deionized water and ethylene glycol. For the vertical alignment mode LC cells, the LC with negative dielectric anisotropy (MLC-2037, Merck) was used. The cell thickness was maintained using glass spacers of $5.0 \pm 0.2 \mu\text{m}$ thick. The LC was injected into the empty cell by capillary action in the isotropic state. The LC textures were observed using a polarized optical microscope (POM) (Potiphot-Pol, Nikon). The voltage-dependent transmittance was measured as a function of the polar angle (θ) using a spatial photometer (EZcontrast 160R, ELDIM). The capacitance of the AVDL was measured in a metal-insulator-metal (aluminum-AVDL-aluminum) structure using an impedance analyzer (HP 4192A, Agilent Technology). Here, the voltage-dependent transmittance from the LC cell without the AVDL was also measured as a reference. After that, gamma curves were obtained from the both cells.

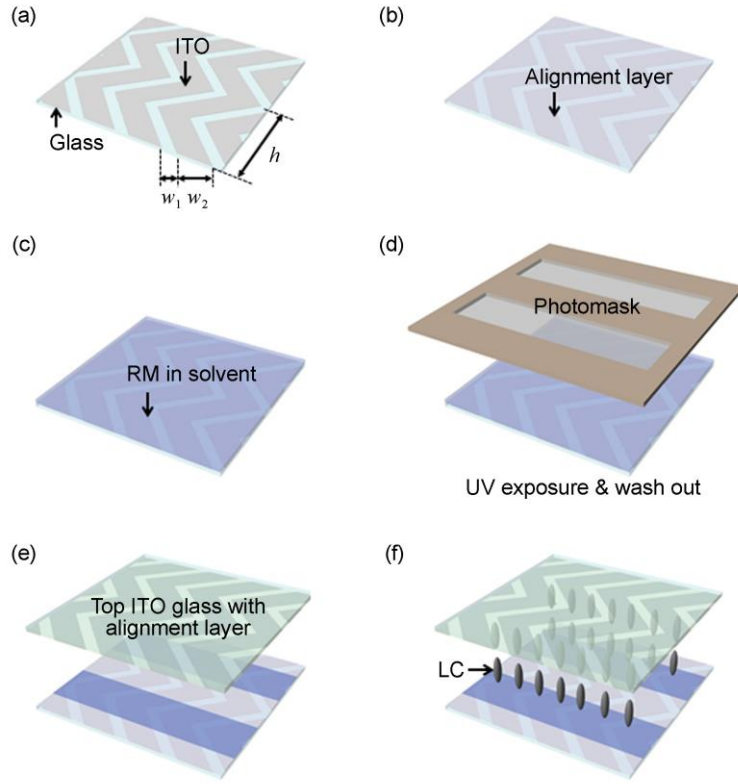


Figure 4.4. Schematic diagram showing the fabrication process of the PVA LC cell based on the AVDL. (a) The patterned ITO glass. Here, w_1 , w_2 , and h are 12 μm , 63 μm , and 150 μm , respectively. The shape of the electrode is identical to the simulation geometry. (b) Deposition of the homeotropic alignment layer by the spin-coating process. (c) Deposition of RM by the spin-coating process. (d) Photopolymerization of RM and wash out process for removal the un-polymerized RM. (e) Construction of the cell with the top patterned ITO glass with the homeotropic alignment layer. (f) Infiltration of LC.

4.4.2 Results and discussion

Surface characteristic of AVDL

Figure 4.5(a) shows the alignment property of LC on the AVDL together with the surface AFM images in conditions of UV exposure time. Interestingly, the alignment of LC was found to become more uniform as the exposure time increases while the roughness variation of each AVDL was relatively small. Figure 4.5(b) shows the surface energies of each AVDL calculated from the contact angles of deionized water and ethylene glycol. Note that the decrease of the surface energy can lead to the homeotropic alignment of LC [39, 49-51]. In our case, however, the reduction of total surface energy arising from the increase of non-polar interaction sites by the cross-linking process was very small to explain the noticeable change of LC alignment property. Thus, it might rather be inferred that the rigidity of the AVDL after the photo-polymerization is strongly related to the alignment uniformity of LC. More precisely, in contact with the partially polymerized RMs [52], molecular order of LC can be broken by the aggregation of RMs.

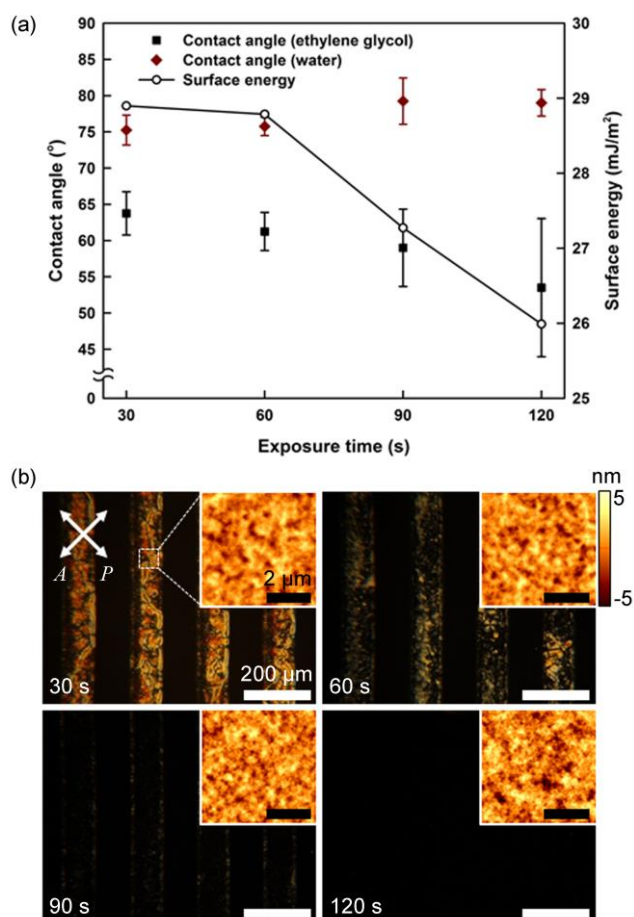


Figure 4.5. (a) Contact angles of deionized water and ethylene glycol together with the corresponding surface energy of the AVDL as a function of the UV exposure time. (b) Microscopic textures of the vertical alignment mode LC cell with periodic AVDLs prepared under four different UV exposure times of 30, 60, 90, and 120 s. Insets show the AFM images of the AVDLs. The values of the surface roughness for the ADVLs were 1.292 nm, 1.288 nm, 1.332 nm, and 1.603 nm. The microscopic textures were taken under crossed polarizers. Scale bars in the inset are 2 μm.

Voltage-dependent transmittance

Figure 4.6 shows the numerical simulations and experimental results for the voltage-dependent transmittance for several different values of the AVDL thickness (d_1). In the presence of the AVDL, the effective voltage (V_e) applied to the LC is given as follows [43]

$$V_e = \frac{\varepsilon_1 d_2}{\varepsilon_1 d_2 + \varepsilon_{||} d_1} V_a = \frac{1}{\beta} V_a. \quad (4.7)$$

Here, V_a is the applied voltage, ε_1 denotes the dielectric constant of the AVDL, and the β represents a scaling factor. Under the strong anchoring condition, the threshold voltage (V_{th}) in the vertical alignment configuration with the AVDL can be written as [1]

$$V_{th} = \beta \pi \sqrt{\frac{K_{33}}{|\Delta\varepsilon|\varepsilon_0}}, \quad (4.8)$$

where ε_0 denotes the permittivity in free space. In our case, the value of V_{th} was simply defined as the voltage at which the transmittance was 2% of the maximum value. For the case of $d_1 = 0.65 \mu\text{m}$, the theoretical value of $V_{th} = 2.85 \text{ V}$ with $\beta = 1.187$ from the numerical simulations in Fig. 4.6(a) and the measured value $V_{th} = 2.95 \text{ V}$ with $\beta = 1.156$ from the experimental results in Fig. 4.6(b). The small difference of V_{th} was due to the thickness variations of the AVDL. Since the total thickness of the LC cell (d) was fixed, the increase of d_1 resulted in the decrease of the LC layer (d_2), meaning that the amount of the phase retardation was changed according to $\Delta n d_2$ through the LC layer.

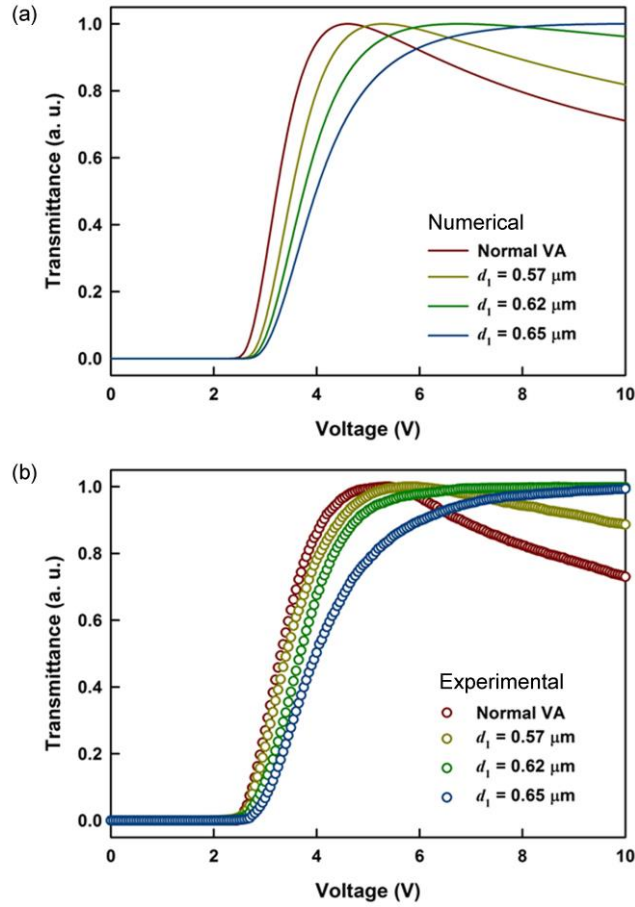


Figure 4.6. (a) The simulation results and (b) the experimental results for the voltage-dependent transmittance of the vertical alignment mode LC cells with different values of the AVDL thickness.

Microscopic images

Figure 4.7 shows the microscopic textures of the LC cell with periodic AVDLs, observed using the POM under crossed polarizers, at different values of the applied voltage (0, 2.5, 3.0, 3.5, 4.0, and 5.0 V). The thickness of the AVDL was determined to be $d_1 = 0.57 \mu\text{m}$. Under no applied voltage, a highly uniform dark

state was obtained. As the applied voltage was gradually increased, the remaining surfaces and sub-domains on the AVDL were successively appeared due to the difference in the threshold voltage between them by the principle of the voltage division.

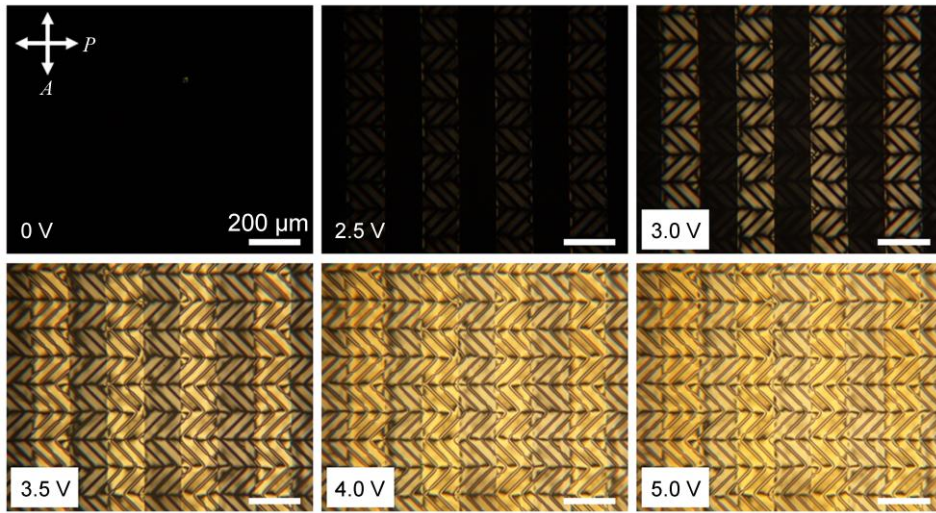


Figure 4.7. (a) Microscopic images of the PVA LC cell with periodic AVDLs ($d_1 = 0.57 \mu\text{m}$) at various applied voltages of 0, 2.5, 3.0, 3.5, 4.0, and 5.0 V. The microscopic textures were taken under crossed polarizers.

Experimental result of gamma distortion

Figures 4.8(a) and 4.8(b) show the experimental results for the gamma curves of the LC cells with $d_1 = 0 \mu\text{m}$ and $d_1 = 0.57 \mu\text{m}$, respectively. The general features of the observed gamma distortions were found to agree well with the simulation results shown in Figs. 5(a) and (b). Clearly, in the presence of the AVDL ($d_1 = 0.57$

μm), the reduction of the GDI was profound at large viewing angles as shown in Fig. 4.8(c). This result is quite desirable since the human eye is more sensitive to change in dark. From the values of GDI shown in Fig. 4.8(c), it was also observed that the relief of gamma shift becomes more distinct at the higher value of the polar angle. It means that the variation of the optical phase retardation depending on the polar angle was successfully diminished by the two different tilt angles of LC in the presence of an applied voltage. In other words, by the use of the AVDL, the gamma shift, particularly at large viewing angles becomes greatly diminished so that the color uniformity at different viewing angles will be preserved.

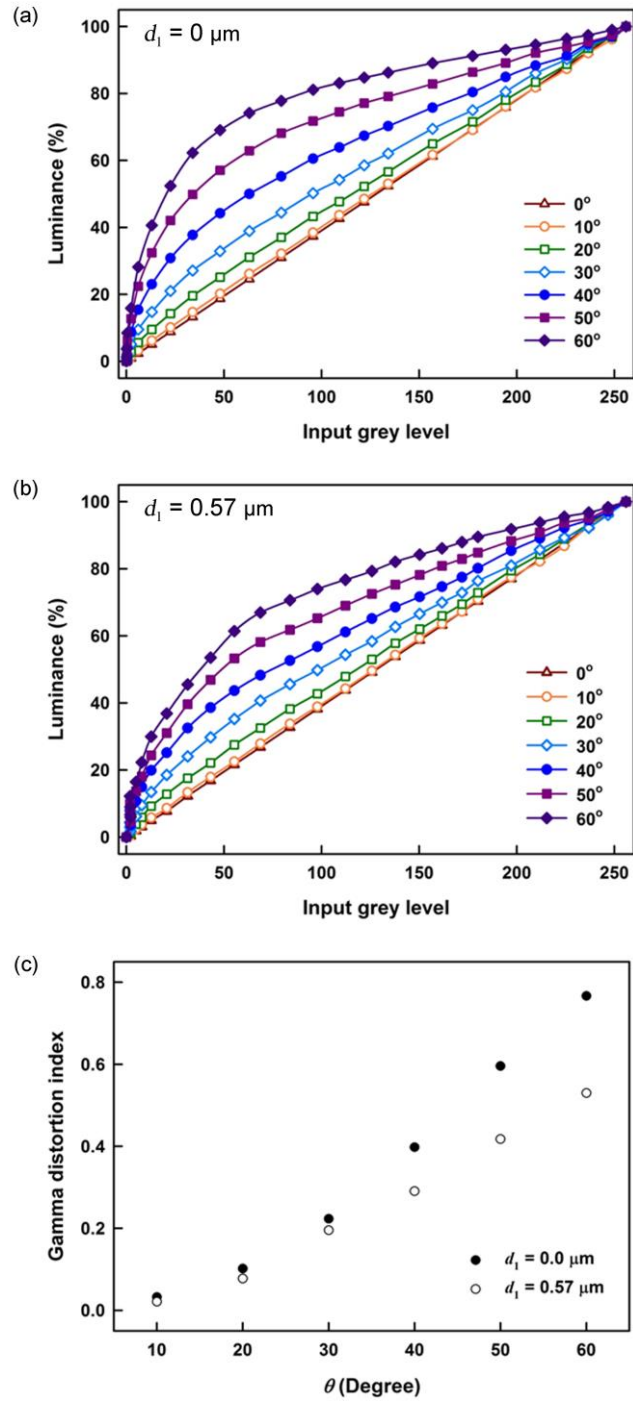


Figure 4.8. Experimental results for the luminance as a function of

the input grey level (gamma curves) for (a) $d_1 = 0 \text{ }\mu\text{m}$ and (b) $d_1 = 0.57 \text{ }\mu\text{m}$. (c) Measured values of the GDI in the case of $d_1 = 0 \text{ }\mu\text{m}$ and $d_1 = 0.57 \text{ }\mu\text{m}$ as a function of the polar angle.

4.5 Summary

In this chapter, it was demonstrated that the new concept of the LCD which enables to reduce gamma distortion at off-axis by forming the AVDL on the homeotropic alignment surface. The AVDL plays a role of the capacitive element in series to divide the applied voltage, providing the sub-domain with the different threshold voltages. In contrast to the conventional multi-domain LCD based on the IVDL, the highly uniform alignment state of LC was realized by the control of the exposure time during photo-polymerization of the AVDL without any planarization process. It is found that GDI is determined by not only the angular distribution of the phase retardation but also the ratio of the transmittance from each sub-domain. The experimental results for the gamma curves of the fabricated LC cell with the AVDL were in good agreement with the numerical calculations. This simple approach is directly applicable for constructing in various types of the LCD modes with high image quality.

Chapter 5

Colloidal Assembly on Wrinkled Template of Reactive Mesogen

5.1 Introduction

RMs have been widely used for many electro-optical applications [53-56] and displays [57-59] due to their capability of constructing polymer networks with optical anisotropy. The use of the RMs has been primarily focused on tuning the electro-optical properties at a mesoscopic level through doping in host materials such as LCs [56, 59-61]. Moreover, the intrinsic anisotropic mechanical properties of the RMs associated with the molecular order enable to produce functional RM

systems showing structure transformation [62-64], shape memorization [65-67], and surface topographies [68-70]. Among them, the wrinkled patterns of the RMs [68, 69] have great potential for more sophisticated templates owing to the easy control of direction and the simplicity of fabrication through the directional alignment of the RMs. Most of the previous works were carried out toward achieving the anisotropic elastic properties on the elastomers in the bilayer structure through the stretching and releasing processes [71-74].

In this chapter, the construction of colloidal microwires will be demonstrated using anisotropic assembling templates with periodically wrinkled patterns of the RM. The wrinkled patterns were produced through the polymerization of the RM on an alignment layer by the oxygen plasma treatment [68]. According to the guidance of the wrinkled patterns, PS particles in colloid were self-assembled into microwires through a simple slit-coating process. The dimension of the microwires was found to be predominantly governed by the period of the wrinkled pattern in relation to the particle size. An assembly of the colloidal particles on a two-directional wrinkled pattern was also demonstrated. The two-directional wrinkled pattern of RM was produced on the multi-domain alignment layer which is produced with the help of stamping-assisted rubbing process [75].

5.2 Templates with Wrinkled Patterns of Reactive Mesogen

Fabrication process

Figure 5.1 shows a schematic diagram of the fabrication steps for the templates with the wrinkled patterns of the RM. For the homogeneous alignment of the RM, an alignment layer (AL22620) was first spin-coated at the rate of 3000 rpm for 30 s on a glass substrate and then thermally cured at 180°C for 1 h as shown in Fig. 5.1(a). The alignment layer was subsequently rubbed along the direction of R . The RM solution used in this work was a RMS03-001C and it was spin-coated at the rate of 2000 rpm for 30 s onto the rubbed alignment layer. By the oxygen plasma treatment at the intensity of 150 W under 0.1 torr for 30 s, the RM film were polymerized to produce anisotropic wrinkles along R as shown in Fig. 5.1(b). This wrinkling behaviour can be understood in terms of a buckling instability in the bilayer structure as described above at Chapter 2 (or see ref. [76]). The RM film corresponds to a bilayer structure which is represented by a heavily polymerized thin layer supported on a softly polymerized underlayer during the oxygen plasma treatment. The height (h) and the period (λ) of the wrinkle would depend on the conditions for the plasma treatment as well as the initial thickness of the RM film. The fabrication of a two-directional template defined by two rubbing directions (R_1 and R_2) was shown in Figs. 5.1(c) and 5.1(d). Two different alignment directions were produced through the stamping-assisted rubbing process combined with a sacrificial layer.

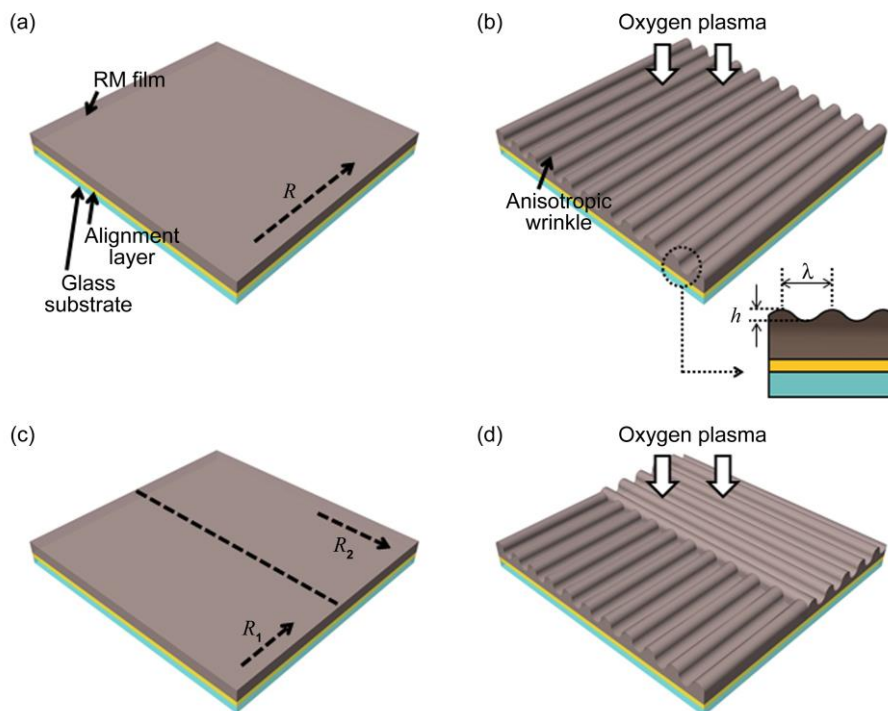


Figure 5.1. Schematic diagram showing the fabrication steps for the templates with the wrinkled patterns of the RM: (a) RMs on an alignment layer with one rubbing direction (R), (b) anisotropic one-directional wrinkled patterns by oxygen plasma treatment together with the wrinkle geometry, (c) RMs on an alignment layer with two rubbing directions (R_1 and R_2), and (d) anisotropic two directional wrinkled patterns by oxygen plasma treatment. The height and the period of the wrinkle are represented by h and λ , respectively.

Wrinkle period depending on RM thickness

Before constructing the assemblies of microwires on the templates, we describe the topography of the wrinkle of the RM and the dependence on the initial thickness of the RM film. The regular one-directional patterns were prepared under several different conditions of the spin-coating rate. The microscopic images of wrinkled patterns are shown in Fig. 5.2(a)-(c). A typical image of a few wrinkled patterns of the RM observed with the AFM is also shown in Fig. 5.2(d). The surface profiles of two patterns of about 1 μm high were shown in the inset. As shown in Figs. 5.2(a)-(c), the period of the wrinkled pattern is varied depending on the spin-coating rate for the deposition of the RM film. Figure 5.2(e) shows the wrinkle period and the wrinkle height variations with the initial thickness of the RM film. For the case of 1000 rpm, λ was about 8 μm while for the case of 6000 rpm, λ was about 4 μm . This structural undulation is primarily related to the stress relaxation in a thermally-induced swelling model [77]. In this model, the increase of the initial film thickness (t) results in the increase of the height (h) and the period (λ) of the wrinkled pattern. While λ was found to monotonically increase with t , h was weakly dependent on t as shown in Fig. 5.2(e). This may be attributed to a relatively small thickness of the underlayer compared to λ and/or a low power of oxygen plasma.

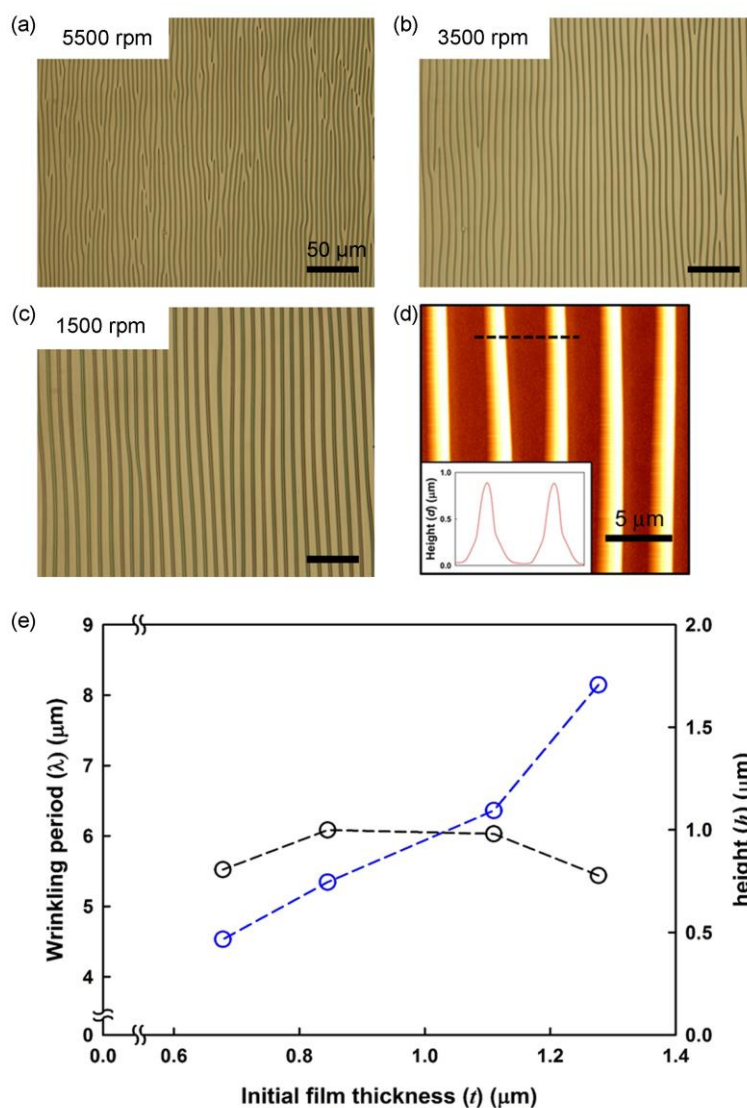


Figure 5.2. (a)-(c) The microscopic images of regular one-directional wrinkle patterns prepared by several conditions of spin-coating rate: (a) 5500 rpm for 30 s, (b) 3500 rpm for 30 s, and (c) 1500 rpm for 30s. (d) The AFM image of a few wrinkled patterns of the RM. The inset shows the surface profiles of two patterns. (e) The wrinkle

period (blue dashed line) and the wrinkle height (black dashed line) variations with the initial thickness of the RM film.

Alignment direction of multi-directional domain

As already shown in Fig. 2.13(c), the two-directional wrinkled patterns of the RM were found to have two orientations being different to initial rubbing directions after polymerization of the RM. One of them is close to the first rubbing direction (R_1) while the other makes an angle between R_1 and the second rubbing direction R_2 . This is probably due to the relaxation of the excess elastic strain produced during the cross-linking of the RMs that might be initially aligned in the orthogonal configuration. In addition, the strength difference between two orthogonal rubbing process can affect the final alignment direction of RM. In fact, alignment direction of the domain rubbed sequentially along R_1 and R_2 can be expressed by sum of two vectors of which direction and length correspond to the rubbing direction and the rubbing strength, respectively. For examining the alignment direction of the orthogonally rubbed multi-domain, homogeneous LC cells were constructed. On the bottom substrate of LC cells, the alignment layer was rubbed along two rubbing directions (R_1 and R_2) using the stamping-assisted rubbing processes. Here, the rubbing strength is controlled by rubbing speed. Note that the increase of duration and/or the repetition of rubbing-process can also increase the rubbing strength. On the top substrate, the alignment layer was simply prepared without rubbing-process. The cell gap was 5 μm and a typical nematic LC (E7, Merck) was injected. Figure 5.3 shows the microscopic images of the multi-directional LC cells. As clearly seen in Fig. 5.3(a) where the second rubbing speed was three times faster than the first rubbing speed, LC was well-aligned along two

orthogonal directions. In case of using similar rubbing speed as shown in Fig. 5.3(b), on the other hand, the LC was aligned obliquely to each other. The alignment direction of LC on the multi-directional domain is approximately 45° with respect to the R_1 .

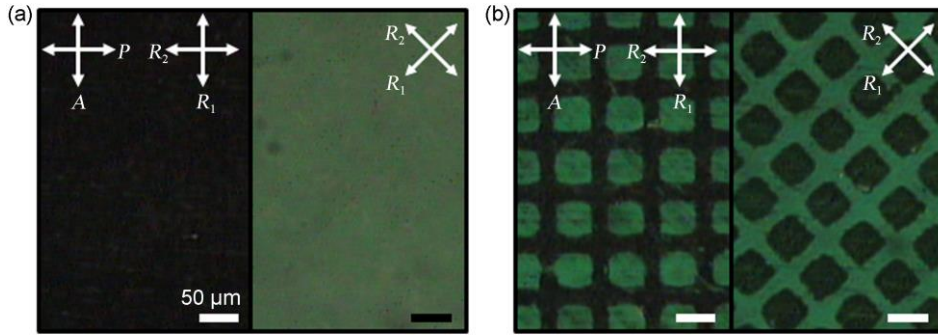


Figure 5.3. The microscopic images of LC texture aligned along two different directions being (a) perpendicular or (b) oblique to each other. The polarizer and the analyzer are denoted by P and A .

5.3 Construction of Colloidal Microwires

For fabricating colloidal microwires, the PS particles dispersed in water (Duke Science) were deposited on the templates by slit-coating process at the speed of 25 $\mu\text{m/s}$. In case of the one-directional wrinkled template, the slit-coating direction is along the direction perpendicular to R and in case of the two-directional wrinkled template, it was perpendicular to R_1

Figure 5.4 show the images of self-assembled colloidal microwires using the PS particles with the width of 1 μm or 2 μm , obtained with a SEM. As described above, it is clear that λ is governed by the initial thickness (t) of the RM film. The value of λ can be easily varied in a range of a few micrometers with varying the spin-coating rate for the deposition of RM film. Here, λ is in range from 4 μm to 7 μm . further increase of λ may be achieved by adjusting the RMs concentration in solution. Depending on λ and the size of the PS particle (r), colloidal microwires in either single line or multiple lines were produced. Note that the uniformity of the colloidal microwires depends on the slit-coating speed. Below a critical value of the slit-coating speed, the colloidal particles are closely packed above the hills of the wrinkles to form multilayer structures [78]. The SEM image showing the colloidal microwires assembled on the template with two orientations of the wrinkled patterns is shown in Fig. 5.4(f). The slit-coating along the oblique direction with respect to the slit-coating direction tends to produce the voids of the particles in lines. On the domain boundaries, the colloidal microwires were poorly defined since the direction of wrinkles patterns were not well distinguished.

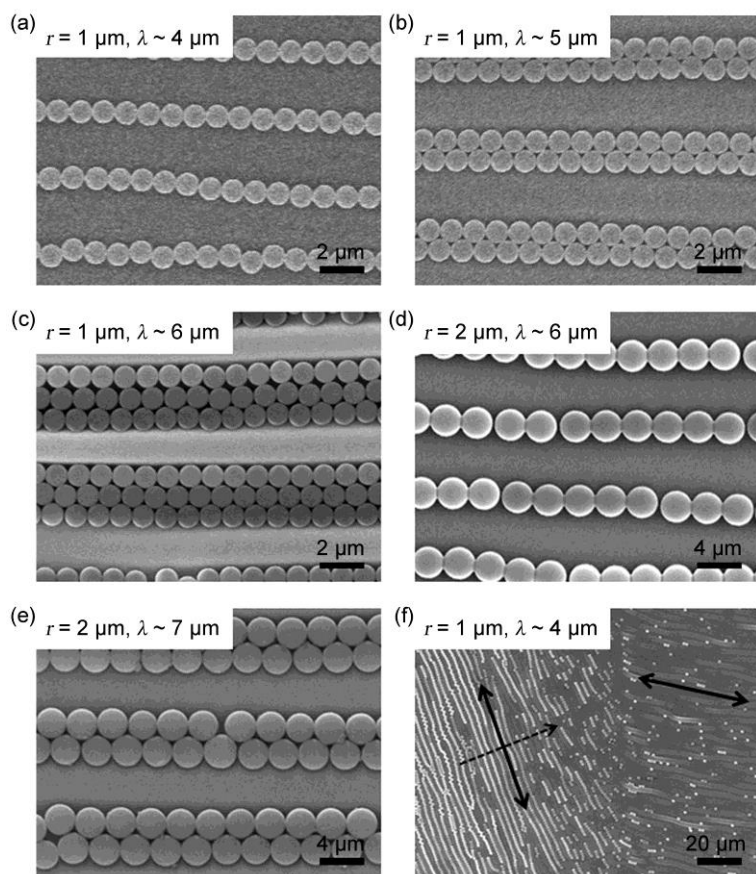


Figure 5.4. The SEM images of single line or multiple lines of colloidal microwires on (a)-(e) the one-directional wrinkled template or (f) the two-directional wrinkled template: (a) $r = 1 \mu\text{m}$, $\lambda \sim 4 \mu\text{m}$ (single line), (b) $r = 1 \mu\text{m}$, $\lambda \sim 5 \mu\text{m}$ (double lines), (c) $r = 1 \mu\text{m}$, $\lambda \sim 6 \mu\text{m}$ (triple lines), (d) $r = 2 \mu\text{m}$, $\lambda \sim 6 \mu\text{m}$ (single line), and (e) $r = 1 \mu\text{m}$, $\lambda \sim 7 \mu\text{m}$ (double lines), and (f) $r = 1 \mu\text{m}$, $\lambda \sim 4 \mu\text{m}$ (single line). Here, black arrow and dashed arrow represent the wrinkle direction and the slit-coating direction, respectively.

5.4 Summary

In this chapter, the assembly of colloidal microwires on the anisotropic wrinkled template of the RM film was demonstrated. The self-organized wrinkles were formed from the aligned RM film through polymerization by the oxygen plasma treatment and used for fabricating colloidal microwires through a simple slit-coating process. Depending on the height and the period of the wrinkle in combination with the particle size, a wide range of microwires in single line or multiple lines can be produced. Moreover, the templates with multiple orientations of the wrinkled patterns, in principle, enable to construct complex networks of colloidal particles. This work will provide a new platform for the bottom-up fabrication of diverse photonic and optoelectronic devices.

Chapter 6

Concluding Remarks

In this thesis, new types of electro-optical devices and the directional assembly of colloidal particles based on the RM were demonstrated. The key concept described in this thesis is the development of the outstanding electro-optical devices and colloidal assembly by utilizing the unique surface characteristics of the aligned RM system.

In Chapter 1, several examples of the LC phase and the basics of RMs were briefly introduced. Especially, the versatility of RMs in both the modification of the functional group and the pattern formation on various surfaces was emphasized.

In Chapter 2, the aligning capability of RM in the LC/RM composite system as well as the RM film polymerized in gradual configuration was experimentally examined as a primal principle covering this thesis. At first, the LC aligning capability of the patterned RM structure formed on the bottom substrate of LC cell was studied. In contrast with the usual LC/polymer composite system where the distortion of LC molecules was observed due to the monotonic directional

preference on the surface of the polymer structure, the highly uniform alignment of LC across the RM patterns was achieved in the LC/RM composite system. It is mainly due to the directional preference of LC on the RM structure is along the molecular orientation of RM. Next, the construction of the RM matrix by surface-initialized polymerization for stabilizing LC was studied. The surface-initialized polymerization process was induced by doping the photo-initiator on the one side of the alignment layer instead of the LC/RM mixture. Both the pure LC layer and stabilized LC layer was then separately formed in the vertical direction of cell. This concept is directly applicable for polymer stabilized electro-optical devices requiring high tuning capability by the external voltage. At last, the self-organized surface topography of the RM film was studied. The surface topography of nano or micro period was provided by varying the speed of the depth-wise gradient polymerization of swelled RM film. In addition, the well-organized wrinkle aligned along the one direction was observed in the aligned RM film when the period of topography increased into micro range.

Based on the studies performed above, a new concept of RLCD based on PSRs was proposed in Chapter 3. The PSR was constructed through the spin-coating of CRM solution, followed by the photo-polymerization process with the photomask. The PSR exhibited the photonic bandgap behaviour which reflects the certain polarization component of the incident light in the pre-defined bandwidth. The reflectance was differed according to the phase retardation of the incident light through an electrically tunable LC layer on the PSR. The reflectance and color purity was found to be greatly improved by the PSR.

In Chapter 4, a new way of reducing gamma distortion in LCD by forming AVDL made of RMs was proposed. AVDL was constructed through a photo-

lithographic patterning process of the deposited RM film with the help of photomask. By using AVDL, highly uniform alignment of the LC molecules can be achieved without any additional surface treatment. It was found that the control of the UV exposure time plays a key role in realizing the stable and uniform homeotropic alignment of the LC molecules across the AVDL. This simple technique enables to produce multi-domains where the shift of the threshold voltage is spontaneously achieved domain by domain in the operation of the voltage division.

Finally, the directional assembly of colloidal microwires on the self-organized surface topography was demonstrated. The uniform periodic wavy structure aligned along the direction of the RM was formed by the plasma treatment for the polymerization. The colloidal microwires in single lines or multiple lines were then assembled on the wavy structure. The number of lines was found to be determined depending on the period of the wrinkle as well as the particle size.

In conclusion, the concept of aligning capability of RM was explored for the control of coloration in advanced electro-optical devices and the colloidal assembly. Based on the experimental results of the unique surface characteristics of aligned RM structure, new types of LCDs as well as construction of colloidal microwires were demonstrated in both the theoretical and the experimental way. This versatile approach will give great impact on the research fields of the advanced electro-optical device and the colloid applications.

Bibliography

- [1] P.-G. d. Gennes and J. Prost, *The physics of liquid crystals*, 2nd ed. (Clarendon Press, Oxford, 1993).
- [2] P. J. Collings, *Liquid crystals: nature's delicate phase of matter* (Princeton University Press, Princeton, 2002).
- [3] V. Chigrinov, ASID'04 Tutorial notes (2004).
- [4] K. K. Kobayashi, Journal of the Physical Society of Japan **29**, 101 (1970).
- [5] J. Clayden, N. Greeves, and S. G. Warren, *Organic chemistry*, 2nd ed. (Oxford University Press, Oxford, 2012).
- [6] C. Allan Guymon, E. N. Hoggan, D. M. Walba, N. A. Clark, and C. N. Bowman, Liquid Crystals **19**, 719 (1995).
- [7] H. Furue, T. Miyama, Y. Iimura, H. Hasebe, H. Takatsu, and S. Kobayashi, Japanese Journal of Applied Physics, Part 2: Letters **36**, L1517 (1997).
- [8] Y. H. Lin, H. S. Chen, H. C. Lin, Y. S. Tsou, H. K. Hsu, and W. Y. Li,

- Applied Physics Letters **96**, 113505 (2010).
- [9] M. Jiao, Y. Li, and S. T. Wu, Applied Physics Letters **96**, 011102 (2010).
- [10] Y. Q. Lu, F. Du, Y. H. Lin, and S. T. Wu, Optics Express **12**, 1221 (2004).
- [11] D. J. Broer, J. Lub, and G. N. Mol, Nature **378**, 467 (1995).
- [12] K.-S. Bae, U. Cha, Y.-J. Lee, Y.-K. Moon, H. C. Choi, J.-H. Kim, and C.-J. Yu, Optics Express **19**, 8291 (2011).
- [13] J.-H. Park, W.-J. Lee, J.-H. Kim, and S.-D. Lee, Japanese Journal of Applied Physics **42**, L1155 (2003).
- [14] X. Zhu, Z. Ge, T. X. Wu, and S.-T. Wu, Journal of Display Technology **1**, 15 (2005).
- [15] Z. Ge, X. Zhu, R. Lu, T. X. Wu, and S.-T. Wu, Applied Physics Letters **90**, 221111 (2007).
- [16] H. Y. Kim, Z. Ge, S.-T. Wu, and S. H. Lee, Applied Physics Letters **91**, 231108 (2007).
- [17] Y. Asaoka, E. Satoh, K. Deguchi, T. Satoh, K. Minoura, I. Ihara, S. Fujiwara, A. Miyata, Y. Itoh, and S. Gyoten, SID Symposium Digest of Technical Papers **40**, 395 (2009).
- [18] T. Yoshioka, T. Ogata, T. Nonaka, M. Moritsugu, S. N. Kim, and S. Kurihara, Advanced Materials **17**, 1226 (2005).

- [19] J. Guo, J. Zhang, Q. Zhang, N. Jiang, and J. Wei, *RSC Advances* **3**, 21620 (2013).
- [20] S. A. Cazzell, M. E. McConney, V. P. Tondiglia, L. V. Natarajan, T. J. Bunning, and T. J. White, *Journal of Materials Chemistry C* **2**, 132 (2014).
- [21] C.-J. Yu, S. I. Jo, Y. J. Lee, and J.-H. Kim, *Molecular Crystals and Liquid Crystals* **594**, 63 (2014).
- [22] S. Y. T. Tzeng, C. N. Chen, and Y. Tzeng, *Liquid Crystals* **37**, 1221 (2010).
- [23] J. Guo, H. Wu, F. Chen, L. Zhang, W. He, H. Yang, and J. Wei, *Journal of Materials Chemistry* **20**, 4094 (2010).
- [24] M. E. McConney, V. P. Tondiglia, J. M. Hurtubise, L. V. Natarajan, T. J. White, and T. J. Bunning, *Advanced Materials* **23**, 1453 (2011).
- [25] A. Y.-G. Fuh, Z.-H. Wu, K.-T. Cheng, C.-K. Liu, and Y.-D. Chen, *Optics Express* **21**, 21840 (2013).
- [26] K. M. Lee, V. P. Tondiglia, M. E. McConney, L. V. Natarajan, T. J. Bunning, and T. J. White, *ACS Photonics* **1**, 1033 (2014).
- [27] X. Zhu, Z. Ge, and S.-T. Wu, *Journal of Display Technology* **2**, 2 (2006).
- [28] B.-J. Mun and G.-D. Lee, *Molecular Crystals and Liquid Crystals* **595**, 92 (2014).

- [29] M. Oh-e and K. Kondo, *Applied Physics Letters* **67**, 3895 (1995).
- [30] S. Lee, S. Lee, and H. Kim, *Applied Physics Letters* **73**, 2881 (1998).
- [31] Y. Tak, W. Park, M. Kim, J. Lee, N. Kim, and J. Souk, *SID Symposium Digest of Technical Papers* **33**, 1281 (2002).
- [32] Y.-J. Lee, S. I. Jo, J.-H. Kim, and C.-J. Yu, *Japanese Journal of Applied Physics* **49**, 030209 (2010).
- [33] J.-H. Na, H. Li, S. C. Park, and S.-D. Lee, *Journal of Information Display* **12**, 191 (2011).
- [34] S. S. Kim, B. H. Berkeley, K. H. Kim, and J. K. Song, *Journal of the Society for Information Display* **12**, 353 (2004).
- [35] J. Ma, Y.-C. Yang, Z. Zheng, J. Shi, and W. Cao, *Displays* **30**, 185 (2009).
- [36] S. B. Park, J.-K. Song, Y. Um, and K.-H. Kim, *Electron Device Letters, IEEE* **31**, 987 (2010).
- [37] K. C. Tien, C. H. Liao, M. H. Wu, W. C. Wei, C. C. Shih, W. H. Hsu, and J. J. Su, *SID Symposium Digest of Technical Papers* **45**, 1481 (2014).
- [38] J.-H. Lee, H. Jin, J.-W. Kim, K.-H. Kim, B. W. Park, T.-H. Yoon, H. Kim, K.-C. Shin, and H. S. Kim, *Journal of Applied Physics* **112**, 054107 (2012).

- [39] J.-H. Suh, J. Kim, Y.-S. Ryu, Y. Sohn, and S.-D. Lee, *Liquid Crystals* **42**, 1236 (2015).
- [40] H. Y. Kim, G. R. Jeon, D.-S. Seo, M.-H. Lee, and S. H. Lee, *Japanese Journal of Applied Physics* **41**, 2944 (2002).
- [41] Y. H. Kwon, J. I. Baek, J. C. Kim, and T. H. Yoon, *Journal of Information Display* **8**, 17 (2007).
- [42] J.-W. Kim, D. H. Song, K.-H. Kim, S.-T. Shin, and T.-H. Yoon, *Applied Optics* **52**, 5256 (2013).
- [43] R. Lu, S.-T. Wu, and S. H. Lee, *Applied Physics Letters* **92**, 051114 (2008).
- [44] S.-W. Choi, H. Jin, K.-H. Kim, J.-H. Lee, H. Kim, K.-C. Shin, H.-S. Kim, and T.-H. Yoon, *Journal of the Optical Society of Korea* **16**, 170 (2012).
- [45] D. W. Berreman, *Philosophical Transactions of the Royal Society of London A: Mathematical, Physical and Engineering Sciences* **309**, 203 (1983).
- [46] C. S. Lee, H. J. Yoon, S. I. Yoon, S. H. Yoon, M. S. Jung, D. W. Kim, and T. Won, *SID Symposium Digest of Technical Papers* **36**, 982 (2005).
- [47] S. J. Hwang, S. M. Kim, Y. J. Lim, S. H. Lee, G.-D. Lee, J.-J. Lyu, and K. H. Kim, *Current Applied Physics* **9**, 556 (2009).
- [48] D. K. Owens and R. Wendt, *Journal of Applied Polymer Science* **13**,

1741 (1969).

- [49] L. T. Creagh and A. R. Kmetz, *Molecular Crystals and Liquid Crystals* **24**, 59 (1973).
- [50] H. J. Ahn, J. B. Kim, K. C. Kim, B. H. Hwang, J. T. Kim, H. K. Baik, J. S. Park, and D. Kang, *Applied Physics Letters* **90**, 253505 (2007).
- [51] S.-J. Hwang, S.-C. Jeng, and I.-M. Hsieh, *Optics Express* **18**, 16507 (2010).
- [52] B. H. Hwang, C. J. Choi, M. K. Jo, J. B. Kim, H. M. Choe, S. S. Chae, Y. S. Kim, and H. K. Baik, *Langmuir* **26**, 5072 (2009).
- [53] H. Kikuchi, M. Yokota, Y. Hisakado, H. Yang, and T. Kajiyama, *Nature Materials* **1**, 64 (2002).
- [54] V. Tondiglia, L. Natarajan, C. Bailey, M. Duning, R. Sutherland, D. Ke-Yang, A. Voevodin, T. White, and T. Bunning, *Journal of Applied Physics* **110**, 053109 (2011).
- [55] J. Kim, Y.-W. Lim, J.-H. Na, and S.-D. Lee, *Applied Optics* **52**, 1752 (2013).
- [56] J.-Y. Hwang, Y.-J. Lee, C. Cho, J. U. Heo, J.-H. Baek, Y. Kim, J.-H. Kim, and C.-J. Yu, *Journal of Physics D: Applied Physics* **46**, 165301 (2013).
- [57] Y.-J. Lee, Y.-K. Kim, S. I. Jo, J. S. Gwag, C.-J. Yu, and J.-H. Kim, *Optics Express* **17**, 10298 (2009).

- [58] D. H. Song, S. R. Lee, T.-H. Yoon, and J. C. Kim, Japanese Journal of Applied Physics **49**, 011702 (2010).
- [59] L. Lu, T. Sergan, V. Sergan, and P. J. Bos, Applied Physics Letters **101**, 251912 (2012).
- [60] F. Castles, F. Day, S. Morris, D. Ko, D. Gardiner, M. Qasim, S. Nosheen, P. Hands, S. Choi, and R. Friend, Nature Materials **11**, 599 (2012).
- [61] S. S. Choi, S. M. Morris, W. T. Huck, and H. J. Coles, Advanced Materials **22**, 53 (2010).
- [62] Y. Yu, M. Nakano, and T. Ikeda, Nature **425**, 145 (2003).
- [63] D. Liu, C. W. Bastiaansen, J. M. den Toonder, and D. J. Broer, Angewandte Chemie International Edition **51**, 892 (2012).
- [64] M. E. McConney, A. Martinez, V. P. Tondiglia, K. M. Lee, D. Langley, I. I. Smalyukh, and T. J. White, Advanced Materials **25**, 5880 (2013).
- [65] H. Jiang, S. Kelch, and A. Lendlein, Advanced Materials **18**, 1471 (2006).
- [66] S. V. Ahir, A. R. Tajbakhsh, and E. M. Terentjev, Advanced Functional Materials **16**, 556 (2006).
- [67] K. M. Lee, H. Koerner, R. A. Vaia, T. J. Bunning, and T. J. White, Soft Matter **7**, 4318 (2011).

- [68] S. H. Kang, J.-H. Na, S. N. Moon, W. I. Lee, P. J. Yoo, and S.-D. Lee, *Langmuir* **28**, 3576 (2012).
- [69] J.-H. Na, S. C. Park, Y. Sohn, and S.-D. Lee, *Biomaterials* **34**, 3159 (2013).
- [70] D. Liu and D. J. Broer, *Angewandte Chemie* **126**, 4630 (2014).
- [71] C. M. Stafford, C. Harrison, K. L. Beers, A. Karim, E. J. Amis, M. R. VanLandingham, H.-C. Kim, W. Volksen, R. D. Miller, and E. E. Simonyi, *Nature Materials* **3**, 545 (2004).
- [72] E. P. Chan and A. J. Crosby, *Soft Matter* **2**, 324 (2006).
- [73] M.-W. Moon and A. Vaziri, *Scripta Materialia* **60**, 44 (2009).
- [74] S. Yang, K. Khare, and P. C. Lin, *Advanced Functional Materials* **20**, 2550 (2010).
- [75] K. Koo, J. H. Na, Y. T. Kim, H. Li, and S. D. Lee, *Journal of Information Display* **10**, 180 (2009).
- [76] Z. Huang, W. Hong, and Z. Suo, *Journal of the Mechanics and Physics of Solids* **53**, 2101 (2005).
- [77] E. P. Chan, S. Kundu, Q. Lin, and C. M. Stafford, *ACS Applied Materials & Interfaces* **3**, 331 (2010).
- [78] K. Chen, S. V. Stoianov, J. Bangerter, and H. D. Robinson, *Journal of Colloid and Interface Science* **344**, 315 (2010).

Publication

1. International paper

1. **S.-U. Kim**, E.-S. Yu, I.-H. Lee, and S.-D. Lee, “Reconfiguring polarization-selective color reflector array based on chiral reactive mesogens”, (Adv. Opt. Mater., in preparation).
2. **S.-U. Kim**, J. Kim, J.-H. Suh, J.-H. Na, and S.-D. Lee, “Concept of active parallax barrier on polarizing interlayer for near-viewing autostereoscopic displays”, (Opt. Express, in preparation).
3. **S.-U. Kim**, B.-Y. Lee, J.-H. Suh, J. Kim, J.-H. Na, and S.-D. Lee, “Reduction of gamma distortions in liquid crystal display by anisotropic voltage-dividing layer of reactive mesogens”, (Liq. Cryst., in press).
4. H.-L. Park, B.-Y. Lee, **S.-U. Kim**, J.-H. Suh, M.-H. Kim, and S.-D. Lee, “Improvement of micro-contact pattern fidelity of organic semiconductors through ultraviolet ozone treatment”, *J. Micro/Nanolith. MEMS MOEMS* **15**, 013501 (2015).

5. **S.-U. Kim**, J. Kim, E.-S. Yu, I.-H. Lee, B.-Y. Lee, and S.-D. Lee, “Colloidal assembling template with wrinkled patterns based on liquid crystalline polymer”, *Mol. Cryst. Liq. Cryst.* **610**, 221 (2015).
6. J. Kim, J.-H. Suh, B.-Y. Lee, **S.-U. Kim**, and S.-D. Lee, “Optically switchable grating based on dye-doped ferroelectric liquid crystal with high efficiency”, *Opt. Express* **23**, 12619 (2015).
7. J.-H. Na, **S.-U. Kim**, Y. Shon, and S.-D. Lee, “Self-organized wrinkling patterns of a liquid crystalline polymer in surface wetting confinement”, *Soft Matter* **11**, 4788 (2015).
8. **S.-U. Kim**, J. Kim, and S.-D. Lee, “Precise Lens-On-Lens Architecture Using Selective Wettability for Image-Depth Representation”, *Mol. Cryst. Liq. Cryst.* **595**, 50 (2014).
9. I.-H. Lee, S.-H. Lee, C.-M. Keum, **S.-U. Kim**, and S.-D. Lee, “Combinational color arrays based on optical micro-resonators in monolithic architecture”, *Opt. Express* **22**, 15320 (2014).
10. **S.-U. Kim**, S. Lee, J.-H. Na, and S.-D. Lee, “Tunable liquid crystal lens array by encapsulation with a photo-reactive polymer for short focal length”, *Opt. Commun.* **313**, 329 (2014).
11. S.-M. Cho, H.-L. Park, M.-H. Kim, **S.-U. Kim**, and S.-D. Lee, “Array of solid-state dye-sensitized solar cells with micropatterned TiO₂ nanoparticles for a high-voltage power source”, *Nanoscale Res. Lett.* **8**, 491 (2012).
12. J.-H. Na, S. C. Park, **S.-U. Kim**, Y. Choi, and S.-D. Lee, “Physical

mechanism for flat-to-lenticular lens conversion in homogeneous liquid crystal cell with periodically undulated electrode”, *Opt. Express* **20**, 864 (2012).

2. Domestic paper

1. J. Kim, **S.-U. Kim**, B.-Y. Lee, J.-H. Suh, and S.-D. Lee, “Lenticular lens array based on liquid crystal with a polarization-dependent focusing effect for 2D-3D image applications”, *J. Inf. Disp.* **16**, 11 (2015).

3. International proceedings

1. S.-D. Lee, J. Kim, H. Kim, **S.-U. Kim**, and C. Kim, “New architectures of liquid crystal-based lenticular lenses in index matching approach for display applications”, *Proc. SPIE* **9769**, 97690L (2016).
2. H.-L. Park, B.-Y. Lee, **S.-U. Kim**, J.-H. Suh, M.-H. Kim, and S.-D. Lee, “Importance of surface modification of a micro-contact stamp for pattern fidelity of soluble organic semiconductors”, *Proc. SPIE* **9568**, 956815 (2015).
3. J. Kim, **S.-U. Kim**, E.-S. Yu, and S.-D. Lee, “Emerging areas for liquid crystal technologies beyond displays”, *SID Int. Symp. Dig. Tech.* **45**, 551 (2014).

4. J.-H. Na, S.-C. Park, **S.-U. Kim**, and S.-D. Lee, “Tunable lenticular lens array using liquid crystal on periodically undulated electrodes for autostereoscopic 2D/3D convertible displays”, *SID Int. Symp. Dig. Tec.* **42**, 1584 (2011).

4. International Conference

1. B.-Y. Lee, I.-H. Lee, **S.-U. Kim**, S. Kang, and S.-D. Lee, “Tribocharge transfer mechanism in conducting polymer-based triboelectric nanogenerators for transparent and flexible energy harvesting devices”, *18th International Conference on Organic Electronics*, Bratislava, Slovakia (2016).
2. **S.-U. Kim**, E.-S. Yu, I.-H. Lee, J. Kim, and S.-D. Lee, “Fabrication of in-cell color patterns based on reactive mesogens for reflective liquid crystal displays”, *16th Topical Meeting on Optics of Liquid Crystals*, Sopot, Poland (2015).
3. I.-H. Lee, E.-S. Yu, **S.-U. Kim**, and S.-D. Lee, “Polarization-dependent color generation by optically anisotropic film in Fabry-Perot cavity”, *16th Topical Meeting on Optics of Liquid Crystals*, Sopot, Poland (2015).
4. I.-H. Lee, S.-H. Lee, **S.-U. Kim**, and S.-D. Lee, “In-cell implementation of Fabry-Perot filter-based color elements into liquid crystal displays”, *16th Topical Meeting on Optics of Liquid Crystals*, Sopot, Poland (2015).

5. **S.-U. Kim**, J. Kim, J.-H. Suh, B.-Y. Lee, and S.-D. Lee, “New vertical alignment mode of liquid crystal display with reduced gamma distortions by periodic patterns of reactive mesogens on alignment layer”, *The 15th International Meeting on Information Display*, Daegu, Korea (2015).
6. E.-S. Yu, **S.-U. Kim**, J.-H. Suh, J. Kim, and S.-D. Lee, “Dependence of the electro-optical properties of vertically aligned liquid crystal device by domain separation of reactive mesogens”, *The 4th Symposium on Liquid Crystal Photonics*, Shenzhen, China (2015).
7. S.-D. Lee, J. Kim, **S.-U. Kim**, B.-Y. Lee, and J.-H. Suh, “Realization of 2D/3D switchable displays with tunable lens array”, *The 4th Symposium on Liquid Crystal Photonics*, Shenzhen, China (2015).
8. J.-H. Suh, B.-Y. Lee, J. Kim, **S.-U. Kim**, and S.-D. Lee, “Wide-range control of liquid crystal anchoring energy based on siloxane oligomer transfer”, *The 2nd Asian Conference on Liquid Crystal*, Busan, Korea (2015).
9. J. Kim, **S.-U. Kim**, B.-Y. Lee, J.-H. Suh, and S.-D. Lee, “Imprinted lenticular lens array based on liquid crystal for autostereoscopic 2D/3D switchable display”, *The 14th International Meeting on Information Display*, Daegu, Korea (2014).
10. **S.-U. Kim**, J. Kim, E.-S. Yu, B.-Y. Lee, and S.-D. Lee, “Multi-directional colloidal assembly on wrinkled liquid crystalline

polymer template”, *25th International Liquid Crystal Conference*, Dublin, Ireland (2014).

11. J. Kim, J.-H. Suh, **S.-U. Kim**, and S.-D. Lee, “All-optically switchable grating based on dye-doped ferroelectric liquid crystal in photo-polymerized structure”, *25th International Liquid Crystal Conference*, Dublin, Ireland (2014).
12. B.-Y. Lee, J. Kim, **S.-U. Kim**, and S.-D. Lee, “Capacitive pressure sensor based on porous hydrophobic elastomer for flexible electronic applications”, *European Materials Research Society Spring Meeting*, Lille, France (2014).
13. J. Kim, **S.-U. Kim**, E.-S. Yu, and S.-D. Lee, “Emerging areas for liquid crystal technologies beyond displays”, *SID Display Week*, San Diego, California, USA (2014).
14. S.-D. Lee, J. Kim, and **S.-U. Kim**, “How to design liquid crystal-based lenses for display applications”, *The 3rd Symposium on Liquid Crystal Photonics*, Shanghai, China (2014).
15. S.-D. Lee, J. Kim, and **S.-U. Kim**, “From optical devices to biological applications of photo-reactive mesogens”, *15th Topical Meeting on Optics of Liquid Crystals*, Honolulu, Hawaii, USA (2013).
16. **S.-U. Kim**, J.-H. Na, J. Kim, and S.-D. Lee, “Axially symmetric polarizers based on photoreactive mesogens through fluidic engraving”, *15th Topical Meeting on Optics of Liquid Crystals*, Honolulu, Hawaii, USA (2013).

17. J. Kim, **S.-U. Kim**, B.-Y. Lee, and S.-D. Lee, “Electrically switchable square lens array based on liquid crystals”, *15th Topical Meeting on Optics of Liquid Crystals*, Honolulu, Hawaii, USA (2013).
18. **S.-U. Kim**, J.-H. Na, J. Kim, and S.-D. Lee, “Precise lens-on-lens architecture using selective wettability for image-depth representation”, *The 13th International Meeting of Information Display*, Daegu, Korea (2013).
19. J. Kim, **S.-U. Kim**, B.-Y. Lee, and S.-D. Lee, “Liquid crystal-based hybrid optical retarder varying a quarter-to-half wave for three-dimensional displays”, *The 13th International Meeting on Information Display*, Daegu, Korea (2013).
20. S.-M. Cho, H.-L. Park, M.-H. Kim, **S.-U. Kim**, and S.-D. Lee, “Micropatterning of TiOx nanoparticles for integration of solid-state dye-sensitized solar cells”, *Collaborative Conference on 3D and Materials Research*, Jeju Island, Korea (2013).
21. **S.-U. Kim**, J.-H. Na, J. Kim, and S.-D. Lee, “Radial polarizer with continuous optic axis using selective wetting inscription based on a liquid crystalline polymer”, *SPIE Photonics West*, San Francisco, California, USA (2013).
22. S.-D. Lee, J.-H. Na, J. Kim, S. C. Park, and **S.-U. Kim**, “Tunable liquid crystal lens array for three-dimensional displays”, *4th Workshop on Liquid Crystals for Photonics*, Hong Kong (2012).
23. **S.-U. Kim**, J.-H. Na, J. Kim, and S.-D. Lee, “Fabrication of

polymer-based dual microlens with high numerical aperture through UV inscription and selective wetting”, *International Symposium on Electronics/Optic Functional Molecules*, Shanghai, China (2012).

국문 초록

반응성 메소겐은 액정 물질 고유의 비등방성을 가지고 있는 동시에 경화를 통해 매우 안정된 액정 고분자 구조를 형성할 수 있는 장점을 가지고 있어 다양한 분야에서 관심을 받고 있다. 반응성 메소겐은 분자 구조를 변형하거나 특정 기능을 가진 작용기를 결합시키는 방식으로 감광성, 감열성 등의 기능을 가질 수 있으며 기관의 종류에 상관없이 단순한 용액 공정을 통해 필름을 형성할 수 있다. 또한 반응성 메소겐 필름의 표면 특성은 반응성 메소겐의 정렬 방향에 따라 달라진다. 이러한 비등방적 표면 성질은 일반적인 고분자들의 등방적 성질과 구별되는 가장 중요한 특징이다.

본 논문에서는 반응성 메소겐의 비등방성을 바탕으로 액정/반응성 메소겐의 복합 구조 또는 표면 지형을 가지는 반응성 메소겐 단일 구조를 제작하여 새로운 개념의 광학 소자 및 일정한 방향을 가지는 마이크로 콜로이드 조립을 제안한다. 우선 패터닝된 액정 고분자 구조물이 하부 기관에 형성되어 있는 액정/액정 고분자 복합 구조에서 반응성 메소겐의 분자 정렬과 액정 배향 관계의 상관관계를 밝혔다. 일반적인 액정/고분자 복합 구조에서는 고분자의 등방적 표면 성질로 인해 액정이

고분자 표면에서 단일한 방향 선호를 가지게 되므로, 다른 방향을 향한 표면간 경계에서 배향 왜곡이 나타나게 된다. 반면 반응성 메소겐 경화를 통해 형성된 액정 고분자 구조물의 표면에서는 액정이 반응성 메소겐의 분자 정렬과 동일한 방향으로 배향하려고 하기 때문에 표면간 경계에서 매우 균일한 액정 배향을 얻을 수 있다. 다음으로, 표면 경화 유도를 통한 액정 안정화에 대하여 살펴보았다. 고분자 주형을 통한 액정 안정화는 주로 경화 유도체가 반응성 메소겐과 함께 액정과 섞여있어 외부 에너지에 노출된 전 영역에서 동시 다발적으로 이루어졌었다. 본 연구에서 제안하는 방식은 경화 유도체가 한쪽 배향막에 첨가되어 외부 에너지에 노출 시 반응성 메소겐이 한쪽 표면에서만 경화된다. 따라서 시편 내부에 수직한 방향으로 단일한 액정 층과 고분자로 안정된 액정 층이 공존하게 된다. 이러한 접근 방식은 외부 전압에 대한 높은 조율도가 필요한 전기 광학적 장치에 적용될 수 있다. 또한 반응성 메소겐 필름의 표면에서 자가 조직화하는 표면 지형에 대하여 살펴보았다. 반응성 메소겐 필름이 팽창한 상태에서 경화도 차이가 수직한 방향으로 유도되었을 때, 수축하는 과정에서 좌굴 불안정성이 발생하여 표면에 지형이 생기게 된다. 이 때, 경화도의 차이에 따라 나노 크기에서부터 마이크로 크기까지 다양한 표면 지형이 형성되는 것을 확인할 수 있다. 경화 전 반응성 메소겐이 정렬되어 있을 때 이러한 표면 지형은 그 크기에 따라 방향성을 가지게 된다.

이러한 실험 결과를 응용하여 우선 새로운 개념의 반사형 액정 표시장치를 제안하였다. 일반적인 반사형 액정 표시장치에서는 색을 선택하는 색 필터와 입사한 빛을 반사시키는 거울이 각각 장치의 상부,

하부에 분리되어 형성되어 있다. 이 방식은 빛이 입사 시와 반사 시 색 필터를 두 번 지나치게 되고, 입사한 빛의 각도 차이에 따라 서로 다른 색 필터를 지나쳐 가기 때문에 반사도와 색 순도가 낮았다. 본 논문에서 제안하는 방식은 편광 반사판을 장치 하부 기관에 형성하여 색 선택과 반사를 동시에 수행한다. 편광 반사판은 액정 시편 하부 기관에 카이랄 네마틱 상을 가진 반응성 메소겐 혼합 용액을 도포하고 광식각하여 형성되었다. 이렇게 제작된 편광 반사판은 특정 파장 영역에 위치하는 빛의 원편광 성분만 반사시키게 되고, 외부 전압에 따라 편광 반사판 상부에 위치한 액정 층에서 위상 지연이 변하게 되어 반사도를 조절 할 수 있다. 이 방식을 이용하여 반사형 액정 표시장치의 반사도와 색 순도를 매우 향상 시킬 수 있었다.

다음으로, 비등방성 전압 분할 층을 이용하여 액정 표시장치에서 감마 왜곡을 감소시키는 새로운 방식을 제안하였다. 감마 왜곡을 완화시키기 위해 액정 표시 장치 내에 전압 분할 층을 형성시킬 경우, 전압 분할 층 주변에서 액정의 배향 왜곡이 발생하여 반드시 평탄화 과정이 추가적으로 필요하였다. 본 논문에서 제안하는 방식은 전압 분할 층을 반응성 메소겐을 이용하여 제작하여 추가적인 평탄화 과정 없이 매우 균일한 액정 배향을 얻을 수 있다. 패터닝 수직 배향 구조에서 비등방성 전압 분할층 도입을 통한 감마 왜곡 완화를 수치적 방법과 실험적 방식을 이용하여 분석하였다.

마지막으로 반응성 메소겐 필름의 자가 조직한 표면 지형을 이용하여 콜로이드 마이크로와이어 조립을 수행하였다. 정렬된 반응성 메소겐 표면에 형성된 마이크로 크기의 지형은 일정한 방향의 매우 균일한 물질

모양을 가지게 된다. 이 지형 위에서 슬릿 코팅 방식을 이용하여 단일 줄 또는 여러 줄의 콜로이드 마이크로와이어를 조립하였다. 콜로이드 마이크로와이어의 개수는 물결의 주기와 콜로이드 입자의 크기에 따라서 결정된다.

결론적으로, 본 논문에서는 반응성 메소겐의 비등방적 정렬 특성을 실험적으로 확인하고 이를 응용한 전기광학 소자 및 콜로이드 조립에 대해 기술하였다. 본 연구에서 제시하는 접근 방식은 다양한 응용 분야에 유용하게 접목되어 기술 진보에 이바지할 것이다.

주요어: 액정, 반응성 메소겐, 액정 표시장치, 반사형 액정 표시장치, 액정/반응성 메소겐 복합 구조, 콜로이드 조립, 자가 조직한 표면 지형

학번: 2010-20771